Master's thesis
Theoretical physics

Reducing systematic uncertainties of the trigger in the charged Higgs boson $H^+ \to \tau_h \nu$ analysis

Antti O. Autio

September 14, 2020

Supervisor(s): Dr. Sami Lehti

Censor(s): Dr. Sami Lehti
Prof. Kenneth Österberg

UNIVERSITY OF HELSINKI
TCM Master's Programme

P.O. Box 42 (Gustaf Hällströmin katu 2)
FI-00014 University of Helsinki

HELSINGIN YLIOPISTO — HELSINGFORS UNIVERSITET — UNIVERSITY OF HELSINKI

Tiedekunta — Fakultet — Faculty	Koulutusohjelma — Utbildningsprogram — Education programme
Faculty of Science	TCM Master's Programme

Tekijä — Författare — Author
Antti O. Autio

Työn nimi — Arbetets titel — Title

Reducing systematic uncertainties of the trigger in the charged Higgs boson $H^+ \to \tau_h \nu$ analysis

Opintosuunta — Studieinriktning — Study track
Theoretical physics

Työn laji — Arbetets art — Level	Aika — Datum — Month and year	Sivumäärä — Sidoantal — Number of pages
Master's thesis	September 14, 2020	65 pages

Tiivistelmä — Referat — Abstract

Hiukkasfysiikan standardimalli kuvaa alkeishiukkasia ja niiden välisiä vuorovaikutuksia. Higgsin bosonin löydön (2012) jälkeen kaikki standardimallin ennustamat hiukkaset on havaittu. Standardimalli on hyvin tarkka teoria, mutta kaikkia havaittuja asioita ei voida kuitenkaan selittää standardimallin puitteissa.

Supersymmetria on yksi houkutteleva tapa laajentaa standardimallia. Matalan energian supersymmetriaa ei kuitenkaan ole havaittu. Supersymmetria vaatii toimiakseen niin sanotun kahden Higgsin dubletin mallin. Tavallisessa standardimallissa on yksi Higgsin dublettikenttä. Higgsin dubletissa on kaksi kompleksista kenttää eli yhteensä neljä vapausastetta, joten voisi olettaa, että siitä syntyy neljä hiukkasta. Kolme vapausasteista kuitenkin sitoutuu välibosoneihin W^+, W^- ja Z, jolloin jäljelle jää yksi Higgsin bosoni.

Kahden Higgsin dubletin malleissa dublettikenttiä on kaksi. Koska se lisää teoriaan yhden neljän vapausasteen dubletin, Higgsin hiukkasia on siinä kaiken kaikkiaan viisi: kolme sähköisesti neutraalia (h, H ja A) sekä kaksi sähköisesti varattua (H^+ ja H^-). Tässä työssä keskitytään varattujen Higgsin hiukkasten etsintään malliriippumattomasti.

Tutkimuksessa käytetään LHC-kiihdyttimen (Large Hadron Collider, suuri hadronitörmäytin) CMS-ilmaisimen (Compact Muon Solenoid, kompakti myonisolenoidi) keräämää dataa. Sähkövarauksellisten Higgsin bosonien etsintä keskittyy lopputiloihin, joissa varattu Higgsin bosoni hajoaa hadroniseksi tau-leptoniksi (eli tau-leptoniksi, joka puolestaan hajoaa hadroneiksi) sekä taun neutriinoksi.

Niin sanottu liipaisu on tapa suodattaa dataa tallennusvaiheessa, sillä dataa tulee törmäyksistä niin paljon, ettei kaiken tallentaminen ole mahdollista. Eri liipaisimet hyväksyvät törmäystapauksia eri kriteerien perusteella. Liipaisusta aiheutuu merkittäviä systemaattisia epävarmuuksia. Tässä työssä liipaisun epävarmuuksia pyritään pienentämään käyttämällä sellaisia liipaisimia, joiden epävarmuudet ovat pienempiä. Tätä varten analyysi on jaettava riippumattomiin osiin, joiden epävarmuudet käsitellään erikseen. Lopuksi osat yhdistetään tilastollisesti toisiinsa, jolloin kokonaisepävarmuuden oletetaan pienenevän. Tässä työssä tutkitaan, pieneneekö tämä epävarmuus ja kuinka paljon.

Näitä menetelmiä käyttäen kykenimme löytämään pieniä parannuksia analyysin tarkkuuteen raskaiden varattujen Higgsin bosonien kohdalla. Lisäksi odotettu raja, jota suurempi varatun Higgsin hiukkasen tuotto tässä lopputilassa olisi havaittavissa, paranee yllättävästi. Tätä rajan paranemista tutkitaan liipaisua emuloimalla. Työ on tarkoitus sisällyttää koko Run2:n datasta julkaistaviin tuloksiin.

Avainsanat — Nyckelord — Keywords
charged Higgs boson

Säilytyspaikka — Förvaringsställe — Where deposited

Muita tietoja — Övriga uppgifter — Additional information

Contents

1. Introduction

In 2012 the ATLAS (A Toroidal LHC ApparatuS) and CMS (Compact Muon Solenoid) detectors at the Large Hadron Collider (LHC) announced the discovery of a Higgs boson like particle [1] [14]. The Higgs boson was the final missing piece of the Standard Model of particle physics which describes all known particles as well as the electromagnetic, weak and strong interactions.

However, the Standard Model is not a perfect theory. As an example, it does not give any particle candidate which could form dark matter. According to astronomical observations dark matter is thought to account for most of the matter in the universe. To fix problems like this, various extensions of the Standard Model are being studied. These are referred to as Beyond the Standard Model theories.

Among the simplest extensions to the Standard Model are the two-Higgs-Doublet models (2HDM). In those we postulate an existence of two complex Higgs doublet fields instead of just one as in the Standard Model. This grows the total number of Higgs bosons to five: two electrically charged Higgs bosons (H^+ and H^-) and three electrically neutral ones (h, H and A). The two Higgs doublets appear for example as a part of a theory known as supersymmetry. Based on the observations a perfect supersymmetry cannot exist but the symmetry may be broken so that the regular Standard Model particles have more massive superpartners. Supersymmetry could explain many of the problematic aspects of the Standard Model.

The charged Higgs bosons have been searched for in multiple experiments such as in the Large Electron-Positron collider [3], the DØ [2] and CDF [16] experiments in Fermilab as well as the CMS [46] and ATLAS [5] experiments at LHC. These experiments have set lower limits for the charged Higgs boson mass and upper limits for its production rate.

In this thesis we are interested in the charged Higgs boson searches at the CMS, more specifically its decay into a tau lepton and a tau neutrino. We analyze the data recorded in 2016 at 13 TeV, already analyzed in [46], with new methods. Since the processes we are interested in are very rare, we must enrich the signal to increase the signal/background ratio to make them visible.

A very important part of the analysis is the estimation and minimization of uncertainties. The analysis has many different uncertainties which all need to be taken into account when assessing the final results. In this analysis one significant source of uncertainties is the trigger uncertainties. The triggers are the first data filters that work in real time during the data taking.

Our goal was to reduce these trigger uncertainties by replacing the trigger with the combination of multiple triggers using a method called categorization.

The current method for example assumes that the efficiencies of the tau and MET (missing transverse energy) parts are uncorrelated. This can possibly be corrected by the trigger categorization. The results from different categories are combined statistically at the very end of the analysis.

We were able to find some categorization schemes that have a small effect in lowering the uncertainty of the analysis for heavy charged Higgs bosons. Additionally, this method of categorizing triggers proved to have a surprisingly large effect in lowering the expected limits in charged Higgs production in the analysis. In order to understand this better we emulated the trigger categorization with the corresponding offline objects.

2. The Standard Model

The Standard Model of particle physics (SM) is a theory that describes three of the four fundamental forces in the universe: the electromagnetic interaction, the weak interaction and the strong interaction as well as the particles that make up all matter (and antimatter). Only the gravitational interaction is missing from this picture. The Standard Model is a tremendously successful theory and it describes all of the currently observed particles. However, we know that there must exist physics beyond the Standard Model since there are many phenomena that are not explained by the SM.

2.1 Particles and gauge structure

The elementary particles of the Standard Model can be divided into fermions and bosons. Fermions have a half-integer spin and they obey Fermi-Dirac statistics. There are 12 of those in the SM, each with a spin of 1/2: 6 quarks and 6 leptons. All of these have additionally a corresponding antiparticle. The leptons have an electric charge of -1 or 0 and do not observe strong interaction whereas the quarks have fractional charges and interact strongly. The fermions are grouped into three generations, with particles in the same generation sharing similar properties.

The gauge bosons are force-carrying particles that mediate the three fundamental interactions of the SM. These are mathematically described as the generators of the symmetries of the SM. These symmetries appear because the observables of the SM are not the fields themselves but their excitations, the particles. There are multiple ways to get the same observable state from the fields. Therefore we may move from one so-called gauge field to another by a gauge transformation keeping observable physics the same.

The gauge group of the SM is $U(1)_Y \times SU(2)_L \times SU(3)_c$. The electromagnetic interaction between charged particles is mediated by the photon, which is the generator of $U(1)_Y$ where Y is the hypercharge. The weak interaction corresponds to $SU(2)_L$. It affects left-handed particles, which is what the L stands for. $SU(2)_L$ has three generators which correspond to the massive $W^{\pm}$ and Z bosons. The last symmetry, $SU(3)_c$ corresponds to the strong interaction and is mediated by eight gluons. The strong interaction couples to color charge, hence the c. The gluons are massless but carry a color charge, meaning they themselves couple to the strong interaction. Additionally, there is the Higgs boson, which relates to the process by which weak gauge bosons acquire mass. It for example explains the large masses of

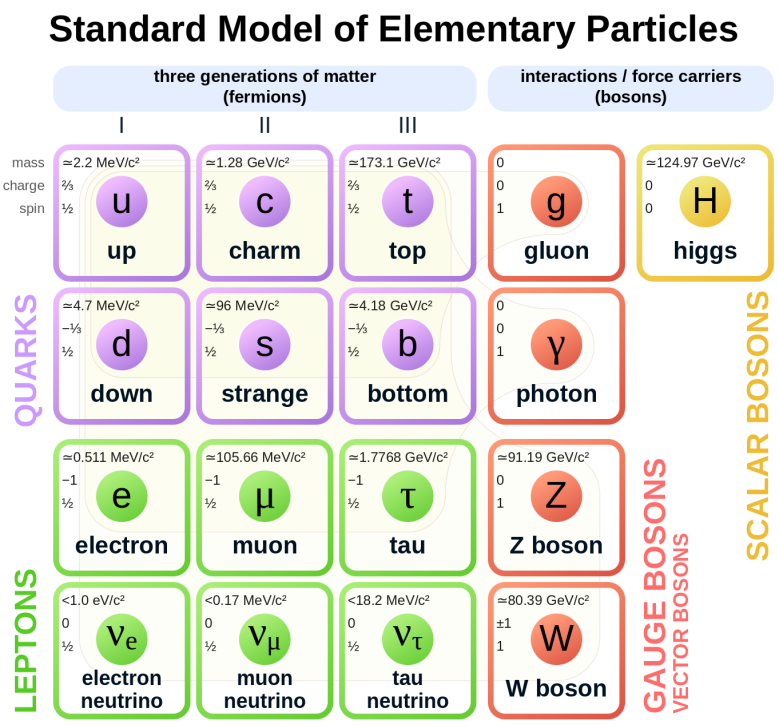

Figure 2.1: The particles of the Standard Model [40]

the W and Z bosons.

2.2 Quantum electrodynamics

Quantum electrodynamics (QED) is the relativistic quantum field theory of the electromagnetic force. It describes how photons interact with matter.

2.2.1 The Dirac Lagrangian

Let us consider the Dirac Lagrangian which describes a free lepton:

$$\mathcal{L}_D = i\bar{\psi}\gamma^\mu\partial_\mu\psi - m\bar{\psi}\psi = \bar{\psi}(i\gamma^\mu\partial_\mu - m)\psi \tag{2.1}$$

Applying the Euler-Lagrange equations to this Lagrangian results in the Dirac equation $i\gamma^\mu\partial_\mu\psi - m\psi = 0$.

The Dirac Lagrangian is invariant under $U(1)$, the group of unitary 1×1 matrices. This corresponds to rotations $e^{iq\alpha}$ on the complex plane. The invariance can be shown explicitly by rotating the fermionic field ψ:

$$\begin{aligned} \psi &\to \psi' = e^{iq\alpha}\psi \\ \bar{\psi} &\to \bar{\psi}' = e^{-iq\alpha}\bar{\psi} \end{aligned} \tag{2.2}$$

Now by plugging the rotated fields into the Dirac Lagrangian, we obtain:

$$\begin{aligned}\mathcal{L}_D \to \mathcal{L}'_D &= \bar{\psi}'(i\gamma^\mu\partial_\mu - m)\psi' \\ &= e^{-iq\alpha}\bar{\psi}(i\gamma^\mu\partial_\mu - m)e^{iq\alpha}\psi \\ &= e^{-iq\alpha}e^{iq\alpha}\bar{\psi}(i\gamma^\mu\partial_\mu - m)\psi \\ &= \bar{\psi}(i\gamma^\mu\partial_\mu - m)\psi \\ &= \mathcal{L}_D\end{aligned} \tag{2.3}$$

The Lagrangian therefore stays invariant under this transformation. Since the parameter α was kept a constant, this is called a *global transformation*. However, we want to impose invariance under *local transformations* as well. This means we promote the parameter α to a function of space-time $\alpha(x)$. We require this since it was shown by 't Hooft [48] that only theories with local gauge invariance are renormalizable. This transforms the Lagrangian in the following way:

$$\begin{aligned}\mathcal{L}_D \to \mathcal{L}'_D &= e^{-iq\alpha(x)}\bar{\psi}(i\gamma^\mu\partial_\mu - m)e^{iq\alpha(x)}\psi \\ &= e^{-iq\alpha}e^{iq\alpha}\bar{\psi}(i\gamma^\mu\partial_\mu - m)\psi - e^{-iq\alpha}e^{iq\alpha}\bar{\psi}\gamma^\mu\psi\partial_\mu\alpha(x) \\ &= \mathcal{L}_D + q\bar{\psi}\gamma^\mu\psi\partial_\mu\alpha(x)\end{aligned} \tag{2.4}$$

The Lagrangian is not invariant since there appears an extraneous term. However, we can fix this by changing the derivative in the expression to the *covariant derivative* D_μ.

$$D_\mu = \partial_\mu + iqA_\mu \tag{2.5}$$

The field A_μ appearing in the above expression must also transform in gauge transformations. Its transformation rule is:

$$A_\mu \to A'_\mu = A_\mu - \partial_\mu\alpha(x) \tag{2.6}$$

Using the Lagrangian with the covariant derivative $\mathcal{L}_{inv} = \bar{\psi}(i\gamma^\mu D_\mu - m)\psi$ and the transformation rules 2.2 and 2.6 we obtain:

$$\begin{aligned}\mathcal{L}_{inv} \to \mathcal{L}'_{inv} &= e^{-iq\alpha(x)}\bar{\psi}(i\gamma^\mu D_\mu - m)e^{iq\alpha(x)}\psi \\ &= e^{-iq\alpha(x)}\bar{\psi}(i\gamma^\mu\partial_\mu - q\gamma^\mu A'_\mu - m)e^{iq\alpha(x)}\psi \\ &= e^{-iq\alpha(x)}e^{iq\alpha(x)}\bar{\psi}(-q\gamma^\mu\partial_\mu\alpha(x) + i\gamma^\mu\partial_\mu - q\gamma^\mu A_\mu + q\gamma^\mu\partial_\mu\alpha(x) - m)\psi \\ &= \bar{\psi}(i\gamma^\mu\partial_\mu - q\gamma^\mu A_\mu - m)\psi \\ &= \bar{\psi}(i\gamma^\mu D_\mu - m)\psi \\ &= \mathcal{L}_{inv}\end{aligned} \tag{2.7}$$

This Lagrangian indeed stays invariant. We can also write this invariant Lagrangian in terms of the original Dirac Lagrangian 2.1 and a new interaction term $\mathcal{L}_{int}$.

$$\mathcal{L}_{inv} = \mathcal{L}_D - q\bar{\psi}\gamma^\mu A_\mu\psi \equiv \mathcal{L}_D + \mathcal{L}_{int} \tag{2.8}$$

2.2.2 Interaction terms

The interaction term corresponds to the coupling between two fermions and a photon. Let's sketch why that is the case, taking electron-photon interaction as an example. We start by defining the *S-matrix* (where S stands for scattering) which is defined by

$$|\Phi(\infty)\rangle = S\,|\Phi(-\infty)\rangle = S\,|i\rangle \tag{2.9}$$

An event can result in many different final states $|f\rangle$ which are all contained within $|\Phi(\infty)\rangle$. The corresponding probability amplitude is

$$\langle f|\Phi(\infty)\rangle = \langle f|S|i\rangle \equiv S_{fi} \tag{2.10}$$

Using the equation of motion in the interaction picture one can obtain an explicit form for the S-matrix in nth order:

$$S^{(n)} = \frac{(-i)^n}{n!}\int ... \int d^4x_1 ... d^4x_n T(\mathcal{H}_{int}(x_1)...\mathcal{H}_{int}(x_n)) \tag{2.11}$$

where T is the time-ordering operator. For tree-level interactions we are merely interested in the first order of the S-matrix.

$$S^{(1)} = -i\int d^4x \mathcal{H}_{int}(x) \tag{2.12}$$

For convenience, we can factor out a delta function implementing four-momentum conservation from the S-matrix and define the Lorentz invariant scattering amplitude $\mathcal{M}_{fi}$.

$$S_{fi} = (2\pi)^4\partial^4(P_f - P_i)i\mathcal{M}_{fi}, \tag{2.13}$$

The matrix element $i\mathcal{M}_{fi}$ will correspond to a Feynman diagram vertex.

Now we may apply this for the interaction Lagrangian 2.8. Conveniently, since the Hamiltonian is defined by

$$\mathcal{H} = \frac{\partial\mathcal{L}}{\partial\dot{\phi}}\dot{\phi} - \mathcal{L} \tag{2.14}$$

and $\mathcal{L}_{int}$ does not depend on the derivatives of fields, $\mathcal{H} = -\mathcal{L}$ and we can simply integrate the interaction Lagrangian.

The explicit forms for the fields are also needed. For fermions we can express this in the basis of solutions to the Dirac equation

$$\psi(x) = \int \frac{d^3p}{(2\pi)^3 2E_p}\sum_{r=1}^{2}[c_{\bar{p},r}u_r(p)e^{-ipx} + d^\dagger_{\bar{p},r}v_r(p)e^{ipx}] \tag{2.15}$$

For the photon field:

$$A^\mu(x) = \int \frac{d^3p}{(2\pi)^3 2E_p}\sum_{\lambda=0}^{3}[\epsilon^\mu(p,\lambda)\alpha_{\bar{p},\lambda}e^{-ipx} + (\epsilon^\mu(p,\lambda))^*\alpha^\dagger_{\bar{p},\lambda}e^{ipx}] \tag{2.16}$$

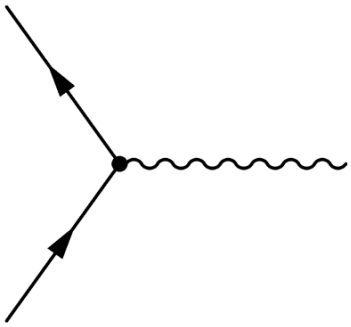

Figure 2.2: The Feynman diagram for a particle and an antiparticle annihilating and producing a photon.

We plug these into 2.12 and integrate over x. The result is:

$$S^{(1)} = (2\pi)^4 \int \frac{d^3p}{(2\pi)^3 2E_p} \frac{d^3p'}{(2\pi)^3 2E_{p'}} \frac{d^3q}{(2\pi)^3 2E_q} \sum_{r,r',\lambda} \left[d_{\bar{p}r} c_{\bar{p}'r'} \alpha^\dagger_{\bar{q}\lambda} (\bar{v}_{rp}(-iq\gamma^\mu)u_{r'p'}) \epsilon^*_{\mu q\lambda} \partial^4(q - p - p') + ... \right] \tag{2.17}$$

where we end up with eight terms of similar structure in total. Let's focus on the first one as an example. There are three operators, a charge-current, a photon polarisation vector and a delta function. In this term there is an electron and a positron and a creation operator for a photon. Therefore the value of S_{fi} is clearly non-zero for this term only when $|i\rangle = |e, p\rangle$ and $|f\rangle = |\gamma\rangle$, i.e. when in the initial state there is an electron and a positron and in the final state just a photon. This term describes an annihilation of an electron-positron pair as seen in Fig 2.2.

From this the value for $\mathcal{M}_{fi}$ for this process can be obtained. Performing the integrations and summations results in

$$i\mathcal{M}_{fi} = (\bar{v}_{r_f p_f}(-iq\gamma^\mu)u_{r_i p_i})\epsilon^*_{\mu q_\gamma \lambda_\gamma} \tag{2.18}$$

The differential cross-section is proportional to $|\mathcal{M}|^2$. This way we can obtain a measurable quantity, the cross-section for an annihilation process. The rest of the terms in equation 2.17 correspond to the other possible interactions of electrons, positrons and photons, such as scattering.

One must remember the interaction term appeared originally because of gauge invariance arguments. So, by requiring the Lagrangian to be invariant under local $U(1)$ transformations, we predicted an interaction.

2.2.3 The photon propagator

This is not the complete QED Lagrangian yet. We are still missing the description of photons by themselves. Therefore we add a third term, $\mathcal{L}_\gamma$, which corresponds to the photon propagator.

$$\mathcal{L}_\gamma = -\frac{1}{4} F^{\mu\nu} F_{\mu\nu} \tag{2.19}$$

Here $F_{\mu\nu}$ is the electromagnetic tensor defined by

$$F_{\mu\nu} = \partial_\mu A_\nu - \partial_\nu A_\mu \tag{2.20}$$

The term $\mathcal{L}_\gamma$ can again be explicitly demonstrated to be gauge invariant under local $U(1)$ transformations.

Now we can finally write the entire QED Lagrangian. The three generations of leptons, which are electrons, muons and taus, have the same coupling to photons so to account for all of those we sum over the leptonic terms.

$$\begin{aligned}\mathcal{L}_{QED} &= \sum_{i=1}^{3}(\mathcal{L}_{D,i} + \mathcal{L}_{int,i}) + \mathcal{L}_\gamma \\ &= \sum_{i=1}^{3}(\bar{\psi}_i(i\gamma^\mu\partial_\mu - m)\psi_i - q\bar{\psi}_i\gamma^\mu A_\mu\psi_i) - \frac{1}{4}F^{\mu\nu}F_{\mu\nu}\end{aligned} \tag{2.21}$$

This describes leptons, photons and interactions between these two types of particles. The coupling strength of the interaction is the coefficient of the interaction term q, which actually is the familiar electric charge. For leptons this is $q = e$, the elementary charge.

2.3 Weak interaction and electroweak unification

The weak interaction is responsible for the radioactive decay of atoms. It was first discovered by Enrico Fermi to explain the β-decay, although he treated it as a 4-point interaction [42]. Since the gauge bosons $W^\pm$ and Z are massive, they decay very quickly, making the 4-point interaction a good approximation at lower energies.

2.3.1 Chirality

The weak interaction is the only interaction violating *parity symmetry* $\mathcal{P}$. The parity operation flips the sign of a spatial coordinate, for example $\mathcal{P}_x x = -x$. The weak interaction also breaks *charge conjugation parity symmetry* CP, which on top of a parity transformation also changes the particle into its antiparticle. This was first experimentally detected by looking at decays of CP-odd K^0 particles decaying into CP-even pions by Christenson *et al* in 1964 [15].

This symmetry breaking leads to the weak force coupling differently to *left-handed* and *right-handed* particles. The handedness is determined by a property called *chirality*. For massless particles it coincides with *helicity*, which is the projection of spin to the direction of the particle's movement. For massive particles helicity depends on reference frame whereas chirality is frame-invariant.

The left- and right-handed fields can be obtained by operating the fields by the fifth Dirac gamma matrix γ^5.

$$\gamma^5 = \begin{pmatrix} 0 & 0 & 1 & 0 \\ 0 & 0 & 0 & 1 \\ 1 & 0 & 0 & 0 \\ 0 & 1 & 0 & 0 \end{pmatrix} \tag{2.22}$$

The left- and right-handed fields have eigenvalues of ± 1 when operated by γ^5. Therefore we may write:

$$\psi = \psi_L + \psi_R \tag{2.23}$$

$$\psi_L = \frac{1}{2}(1 - \gamma^5)\psi \tag{2.24}$$

$$\psi_R = \frac{1}{2}(1 + \gamma^5)\psi \tag{2.25}$$

This also allows us to separate the fermion Lagrangian as well.

$$\mathcal{L} = \mathcal{L}_L + \mathcal{L}_R = \bar{\psi_L}(i\gamma^\mu \partial_\mu - m)\psi_L + \bar{\psi_R}(i\gamma^\mu \partial_\mu - m)\psi_R \tag{2.26}$$

The left-handed fermion fields are now doublets. The left-handed leptons form doublets with neutrinos and quarks with other quarks in the same generation.

$$\begin{pmatrix} \nu_e \\ e \end{pmatrix}_L, \ \begin{pmatrix} \nu_\mu \\ \mu \end{pmatrix}_L, \ \begin{pmatrix} \nu_\tau \\ \tau \end{pmatrix}_L, \ \begin{pmatrix} u \\ d \end{pmatrix}_L, \ \begin{pmatrix} c \\ s \end{pmatrix}_L, \ \begin{pmatrix} t \\ b \end{pmatrix}_L \tag{2.27}$$

The right-handed fields do not observe weak interaction and are therefore just singlets.

$$e_R, \ \mu_R, \ \tau_R, \ u_R, \ d_R, \ c_R, \ s_R, \ t_R, \ b_R \tag{2.28}$$

Right-handed neutrinos have not been observed but if they exist they are their own singlets as well.

2.3.2 Symmetries of the weak interaction

Since the symmetry group of the weak interaction is $SU(2)$, the field must stay invariant when operated by a special unitary 2×2 matrix U for which:

$$UU^\dagger = U^\dagger U = 1, \ \det(U) = 1 \tag{2.29}$$

Since any special unitary group $SU(N)$ has $N^2 - 1$ linearly independent generators, $SU(2)$ has three generators. In fact, the matrices U can be written as

$$U = e^{i\omega_a(x)T^a} \tag{2.30}$$

where ω_a are real parameters and T^a are the generators of $SU(2)$ which can be written as one half times the corresponding *Pauli matrix*.

$$T^1 = \frac{1}{2}\sigma^1 = \frac{1}{2}\begin{pmatrix} 0 & 1 \\ 1 & 0 \end{pmatrix}, \ T^2 = \frac{1}{2}\sigma^2 = \frac{1}{2}\begin{pmatrix} 0 & -i \\ i & 0 \end{pmatrix}, \ T^3 = \frac{1}{2}\sigma^3 = \frac{1}{2}\begin{pmatrix} 1 & 0 \\ 0 & -1 \end{pmatrix} \tag{2.31}$$

These are called the *weak isospin operators*. The weak isospin is the charge of the weak interaction. The operators satisfy the commutation relation

$$[T^a, T^b] = \epsilon_{abc}T^c \tag{2.32}$$

We can test the Dirac Lagrangian's invariance under local $SU(2)$ transformations. All indices of handedness and particle type are omitted for convenience and we'll just consider a generic term.

$$\begin{aligned}\mathcal{L} = \bar{\psi}(i\gamma^\mu\partial_\mu - m)\psi \rightarrow \mathcal{L}' &= \bar{\psi}U^\dagger(x)(i\gamma^\mu\partial_\mu - m)U(x)\psi \\ &= \bar{\psi}(i\gamma^\mu\partial_\mu - m)\psi + i\bar{\psi}\gamma^\mu U^\dagger(x)(\partial_\mu U(x))\psi\end{aligned} \tag{2.33}$$

So the Lagrangian is once again not invariant and we must introduce the covariant derivative. This time it is of the form

$$D_\mu = \partial_\mu \mathbb{1} + ig\mathrm{W}_\mu \tag{2.34}$$

where g is a coupling constant and the gauge field W_μ transforms as

$$\mathrm{W}_\mu \rightarrow \mathrm{W}'_\mu = U(x)\mathrm{W}_\mu U^\dagger(x) + \frac{i}{g}(\partial_\mu U(x))U^\dagger(x) \tag{2.35}$$

Indeed, using this covariant derivative the Lagrangian stays invariant:

$$\begin{aligned}\mathcal{L}' &= \bar{\psi}U^\dagger(x)(i\gamma^\mu D'_\mu - m)U(x)\psi \\ &= \bar{\psi}U^\dagger(x)(i\gamma^\mu(\partial_\mu + ig\mathrm{W}'_\mu) - m)U(x)\psi \\ &= \bar{\psi}U^\dagger(x)U(x)i\gamma^\mu\partial_\mu\psi + \bar{\psi}U^\dagger(x)i\gamma^\mu(\partial_\mu U(x))\psi - \bar{\psi}U^\dagger(x)U(x)g\gamma^\mu\mathrm{W}_\mu U^\dagger(x)U(x)\psi \\ &- \bar{\psi}U^\dagger(x)i\gamma^\mu(\partial_\mu U(x))U^\dagger(x)U(x)\psi - \bar{\psi}U^\dagger(x)U(x)m\psi \\ &= \bar{\psi}i\gamma^\mu\partial_\mu\psi - \bar{\psi}g\gamma^\mu\mathrm{W}_\mu\psi - \bar{\psi}m\psi \\ &= \bar{\psi}(i\gamma^\mu D_\mu - m)\psi = \mathcal{L}\end{aligned} \tag{2.36}$$

Next we want to write the covariant derivative 2.34 explicitly. We can use the generators T^a from 2.31 as a basis for the components of W_μ:

$$D_\mu = \partial_\mu\mathbb{1} + ig\mathrm{W}^a_\mu T_a = \partial_\mu\mathbb{1} + \frac{ig}{2}\begin{pmatrix}\mathrm{W}^3_\mu & \mathrm{W}^1_\mu - i\mathrm{W}^2_\mu \\ \mathrm{W}^1_\mu + i\mathrm{W}^2_\mu & -\mathrm{W}^3_\mu\end{pmatrix} \tag{2.37}$$

The off-diagonal terms correspond to charged-current weak interaction and the physical particles $\mathrm{W}^\pm$. However, it turns out that for the neutral-current weak interaction the physical force-carrier boson Z is a linear combination of the neutral field W^3_μ and another neutral field B_μ. This extra field comes from requiring the Lagrangian to also be $U(1)$ symmetric. Since $U(1)$ is the symmetry group of the electromagnetic force, this allows us to unify these two forces.

2.3.3 The electroweak unification

We require the Lagrangian to be symmetric under $U(1) \times SU(2)$.This corresponds to the transformation

$$\mathrm{U}(x) = e^{i\omega^a(x)T_a + iY\alpha(x)} \tag{2.38}$$

where Y is the *weak hypercharge* which can be written as two times the identity matrix and is defined by

$$Y = 2(Q - T^3) \tag{2.39}$$

where Q is the familiar electric charge.

To achieve local gauge invariance, the covariant derivative is modified by adding an extra term so that

$$D_\mu = \partial_\mu + ig\mathrm{W}_\mu + ig'Y\mathrm{B}_\mu \tag{2.40}$$

where g and g' are coupling constants. As usual, the fields transform as well. The transformation of the field W_μ is already given in equation 2.35 and the field B_μ transforms as follows:

$$\mathrm{B}_\mu \to \mathrm{B}'_\mu = \mathrm{B}_\mu + \frac{iY}{g'}\partial_\mu\alpha(x) \tag{2.41}$$

A standard gauge transformation confirms that with these choices the Lagrangian is indeed invariant under $U(1) \times SU(2)$.

Now we may finally write the entire $U(1) \times SU(2)$ covariant derivative 2.40 in explicit form.

$$D_\mu = \partial_\mu \mathbb{1} + ig\mathrm{W}^a_\mu T_a + ig'\frac{Y}{2}\mathrm{B}_\mu\mathbb{1} = \begin{pmatrix} \partial_\mu + \frac{ig}{2}\mathrm{W}^3_\mu + \frac{ig'}{2}\mathrm{B}_\mu & \frac{ig}{2}(\mathrm{W}^1_\mu - i\mathrm{W}^2_\mu) \\ \frac{ig}{2}(\mathrm{W}^1_\mu + i\mathrm{W}^2_\mu) & \partial_\mu - \frac{ig}{2}\mathrm{W}^3_\mu + \frac{ig'}{2}\mathrm{B}_\mu \end{pmatrix} \tag{2.42}$$

This matrix now describes the electroweak interaction. Note that the fields W^a_μ only couple to left-handed particles.

However, it must be noted that the observed particles do not directly correspond to the fields W^a_μ and B_μ, but their linear combinations. The observed $\mathrm{W}^\pm$ bosons are linear combinations of W^1 and W^2:

$$\mathrm{W}^\pm_\mu = \frac{1}{\sqrt{2}}(\mathrm{W}^1_\mu \mp i\mathrm{W}^2_\mu) \tag{2.43}$$

The mixing between the W^3 and B fields gives the Z boson as well as the photon. It is defined in terms of the *Weinberg angle*:

$$\sin\theta_\mathrm{W} = \frac{g'}{\sqrt{g^2 + g'^2}}, \quad \cos\theta_\mathrm{W} = \frac{g}{\sqrt{g^2 + g'^2}} \tag{2.44}$$

The mixing is then

$$\begin{aligned} \gamma_\mu &= \mathrm{W}^3_\mu \sin\theta_\mathrm{W} + \mathrm{B}_\mu \cos\theta_\mathrm{W} \\ \mathrm{Z}_\mu &= \mathrm{W}^3_\mu \cos\theta_\mathrm{W} - \mathrm{B}_\mu \sin\theta_\mathrm{W} \end{aligned} \tag{2.45}$$

2.4 Quantum chromodynamics

Quantum chromodynamics (QCD) is the theory of the strong interaction, mediated by gluons, which are spin 1 massless bosons. The strong interaction is the force keeping the quarks together to form hadrons. The charge of the strong interaction is called the *color charge*. It appears in three so-called colors: red (r), green (g) and blue (b) and their anticolors $\bar{\mathrm{r}}$, $\bar{\mathrm{g}}$ and $\bar{\mathrm{b}}$.

A neutral combination of these charges is said to be colorless and it is achieved either by having together all three colors or a color and its anticolor. All hadrons

found in nature are colorless because of a phenomenon called *color confinement*. If one tries to separate quarks into non-colorless constituents, the energy required for this is enough to create new quarks, keeping everything colorless in the end.

While quarks have a color charge, antiquarks have an anticolor charge. Therefore we may write a quark as a flavor triplet:

$$q = \begin{pmatrix} q_r \\ q_b \\ q_g \end{pmatrix} \tag{2.46}$$

2.4.1 Gluons

QCD has the symmetry group $SU(3)_c$ so it has 8 generators and there are 8 gluons carrying the force. The generators are called the *Gell-Mann matrices*:

$$\begin{gathered} \lambda_1 = \begin{pmatrix} 0 & 1 & 0 \\ 1 & 0 & 0 \\ 0 & 0 & 0 \end{pmatrix}, \ \lambda_2 = \begin{pmatrix} 0 & -i & 0 \\ i & 0 & 0 \\ 0 & 0 & 0 \end{pmatrix}, \ \lambda_3 = \begin{pmatrix} 1 & 0 & 0 \\ 0 & -1 & 0 \\ 0 & 0 & 0 \end{pmatrix}, \\ \lambda_4 = \begin{pmatrix} 0 & 0 & 1 \\ 0 & 0 & 0 \\ 1 & 0 & 0 \end{pmatrix}, \ \lambda_5 = \begin{pmatrix} 0 & 0 & -i \\ 0 & 0 & 0 \\ i & 0 & 0 \end{pmatrix}, \ \lambda_6 = \begin{pmatrix} 0 & 0 & 0 \\ 0 & 0 & 1 \\ 0 & 1 & 0 \end{pmatrix}, \\ \lambda_7 = \begin{pmatrix} 0 & 0 & 0 \\ 0 & 0 & -i \\ 0 & i & 0 \end{pmatrix}, \ \lambda_8 = \frac{1}{\sqrt{3}} \begin{pmatrix} 1 & 0 & 0 \\ 0 & 1 & 0 \\ 0 & 0 & -2 \end{pmatrix} \end{gathered} \tag{2.47}$$

The gluons can be written for example as the following linear combinations of color-anticolor pairs:

$$\begin{gathered} \frac{\mathrm{r}\bar{\mathrm{b}} + \mathrm{b}\bar{\mathrm{r}}}{\sqrt{2}}, \ \frac{-i(\mathrm{r}\bar{\mathrm{b}} - \mathrm{b}\bar{\mathrm{r}})}{\sqrt{2}}, \ \frac{\mathrm{r}\bar{\mathrm{g}} + \mathrm{g}\bar{\mathrm{r}}}{\sqrt{2}}, \ \frac{-i(\mathrm{r}\bar{\mathrm{g}} - \mathrm{g}\bar{\mathrm{r}})}{\sqrt{2}}, \\ \frac{\mathrm{b}\bar{\mathrm{g}} + \mathrm{g}\bar{\mathrm{b}}}{\sqrt{2}}, \ \frac{-i(\mathrm{b}\bar{\mathrm{g}} + \mathrm{g}\bar{\mathrm{b}})}{\sqrt{2}}, \ \frac{\mathrm{r}\bar{\mathrm{r}} - \mathrm{b}\bar{\mathrm{b}}}{\sqrt{2}}, \ \frac{(\mathrm{r}\bar{\mathrm{r}} + \mathrm{b}\bar{\mathrm{b}} - 2\mathrm{g}\bar{\mathrm{g}})}{\sqrt{6}} \end{gathered} \tag{2.48}$$

All of these are linearly independent and also independent of the forbidden singlet state $\frac{1}{\sqrt{3}}(\mathrm{r}\bar{\mathrm{r}} + \mathrm{g}\bar{\mathrm{g}} + \mathrm{b}\bar{\mathrm{b}})$. The problem with this state is that it would be colorless, making this gluon not experience the strong force itself. This would make the lifetime of the gluon extremely long which would in turn greatly increase the range of the strong force and completely change QCD physics.

2.4.2 The QCD Lagrangian

For QCD we have the following covariant derivative:

$$D_\mu = \partial_\mu + ig_s G_\mu \tag{2.49}$$

The field G_μ can be written in the color basis using the Gell-Mann matrices:

$$G_\mu = \frac{1}{2} \sum_{a=1}^{8} \lambda_a G_\mu^a \tag{2.50}$$

where G^a are real. The transformation rule for G_μ looks familiar from the electroweak case in Eq. 2.35:

$$G_\mu \to U G_\mu U^\dagger + \frac{i}{g_s}(\partial_\mu U)U^\dagger \tag{2.51}$$

with U now being the transformation matrix of $SU(3)$. To write the Lagrangian we'll need the propagation term for the gluons. For this we'll define

$$G_{\mu\nu} = \partial_\mu G_\nu - \partial_\nu G_\mu + i g_s f_{abc} G^b_\mu G^c_\nu \tag{2.52}$$

Here f_{abc} are the structure constants of $SU(3)_c$ defined by the commutation relation:

$$[\lambda_a, \lambda_b] = 2i \sum_{c=1}^{8} f_{abc} \lambda_c \tag{2.53}$$

Written explicitly, this amounts to:

$$\begin{aligned} f_{123} &= 1 \\ f_{458} = f_{678} &= \frac{\sqrt{3}}{2} \\ f_{147} = f_{246} = f_{257} = f_{345} = f_{516} = f_{637} &= \frac{1}{2} \\ f_{ijk} = f_{jki} &= -f_{jik} \\ f_{ijk} &= 0 \text{ for other permutations} \end{aligned} \tag{2.54}$$

Now we can write the dynamical term for the gluon Lagrangian analogously to the photon propagator 2.19, the only difference being the extra term added to the gluon propagator 2.52 for gauge invariance.

$$\begin{aligned} \mathcal{L}_g &= -\frac{1}{4}\sum_{a=1}^{8} G^a_{\mu\nu} G^{\mu\nu}_a \\ &= -\frac{1}{4}(\partial_\mu G^a_\nu - \partial_\nu G^a_\mu)(\partial^\mu G^\nu_a - \partial^\nu G^\mu_a) - \frac{1}{4} g_s^2 f^{abc} f_{ade} G^\mu_b G^\nu_c G^d_\mu G^e_\nu \\ &+ \frac{1}{2} f_{abc}(\partial_\mu G^a_\nu - \partial_\nu G^a_\mu) G^{\mu b} G^{\nu c} \end{aligned} \tag{2.55}$$

The entire QCD Lagrangian is the sum of $\mathcal{L}_g$ and the Dirac Lagrangian using the covariant derivative 2.49:

$$\begin{aligned} \mathcal{L}_{QCD} &= \sum_f \bar{q}_f (i\gamma^\mu \partial_\mu - m_f) q_f - \sum_f g_s \bar{q}_f \gamma^\mu G_\mu q_f \\ &- \frac{1}{4}(\partial_\mu G^a_\nu - \partial_\nu G^a_\mu)(\partial^\mu G^\nu_a - \partial^\nu G^\mu_a) - \frac{1}{4} g_s^2 f^{abc} f_{ade} G^\mu_b G^\nu_c G^d_\mu G^e_\nu \\ &+ \frac{1}{2} f_{abc}(\partial_\mu G^a_\nu - \partial_\nu G^a_\mu) G^{\mu b} G^{\nu c} \end{aligned} \tag{2.56}$$

The first term corresponds to the fermion propagator and the second to the gluon-fermion interaction. After that we have the term for the gluon field propagator

and the last two terms correspond to the gluon 4-point and 3-point self-interactions respectively.

One problem with carrying out QCD calculations is that the coupling is too strong for perturbation theory to be applicable. However, in the high energy regime the coupling strength of the strong interaction weakens, making perturbation theoretic calculations possible. This is known as *asymptotic freedom*.

2.5 The Higgs mechanism

The theory presented so far does not predict the weak gauge bosons $W^{\pm}$ and Z to have masses. However, we know from experiments that these particles actually do have quite high masses. This is caused by something called the Englert-Brout-Higgs-Guralnik-Hagen-Kibble mechanism which we will hereafter refer to as the Higgs mechanism for short. It was independently formulated by Brout and Englert [29], Guralnik, Hagen and Gibble [34] and Higgs [36]. The effect is triggered by the *spontaneous symmetry break* which breaks the electroweak $SU(2)_L \times U(1)_Y$ symmetry, only leaving the symmetry $U(1)_{em}$ intact.

2.5.1 The Higgs potential

To break the symmetry, we will introduce a new doublet consisting of two complex scalar fields:

$$\Phi = \begin{pmatrix} \phi^+ \\ \phi^0 \end{pmatrix} = \frac{1}{\sqrt{2}} \begin{pmatrix} \phi_1 + i\phi_2 \\ \phi_3 + i\phi_4 \end{pmatrix} \tag{2.57}$$

The Lagrangian for a scalar field is of the following form:

$$\mathcal{L}_{scalar} = |D_\mu \Phi|^2 - \mu^2 \Phi^\dagger \Phi - \lambda (\Phi^\dagger \Phi)^2 \tag{2.58}$$

where D_μ is the $SU(2)_L \times U(1)_Y$ covariant derivative from 2.40. We can separate the potential out of the Lagrangian:

$$V(\Phi) = \mu^2 \Phi^\dagger \Phi + \lambda (\Phi^\dagger \Phi)^2 \tag{2.59}$$

The extrema of the potential can be found by calculating the zeros of the derivative.

$$\frac{\partial V}{\partial \Phi^\dagger} = (\mu^2 + 2\lambda \Phi^\dagger \Phi)\Phi = 0 \tag{2.60}$$

To have a ground state the potential should be bound from below, which requires $\lambda > 0$. Now, there are two options. If $\mu^2 > 0$, the only zero is found at $\Phi = 0$ which is a minimum of V. But if $\mu^2 < 0$, things change. There is a maximum at $\Phi = 0$ and a circle of minima at $\Phi^\dagger \Phi = -\mu^2/2\lambda$. This is the case we will be investigating. The potential is visualized in Fig 2.3.

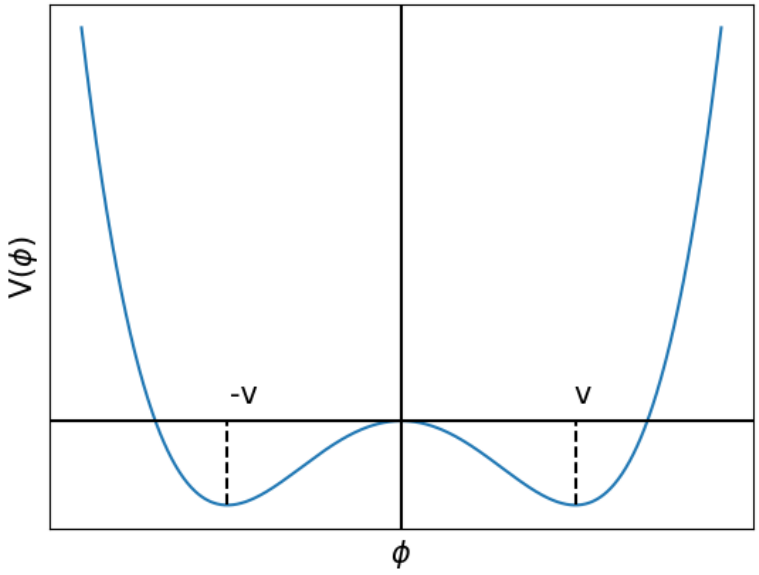

Figure 2.3: A 2D slice of the Higgs potential with $\mu^2 < 0$. The minima can be found at $\pm v$.

2.5.2 Symmetries of the vacuum state

We are free to choose the minimum. From Equation 2.60 we may write the vacuum state (minimum) now as:

$$\langle 0|\Phi^\dagger\Phi|0\rangle = \phi^{+\dagger}\phi + \phi^{0\dagger}\phi^0 = -\frac{\mu^2}{2\lambda} \equiv \frac{v^2}{2} \tag{2.61}$$

The quantity $\langle 0|\Phi^\dagger\Phi|0\rangle$ is called the *vacuum expectation value* or VEV for short. It being nonzero means that the vacuum is actually not empty.

We may arbitrarily (but conveniently) choose one minimum which fulfils 2.61:

$$\begin{aligned} \phi^0_{ground} = 0, \;\; \phi^+_{ground} &= \frac{v}{\sqrt{2}} \\ \Rightarrow \Phi_{ground} &= \frac{1}{\sqrt{2}}\begin{pmatrix} 0 \\ v \end{pmatrix} \end{aligned} \tag{2.62}$$

This corresponds to choosing the so-called *unitary gauge*.

We can explicitly check how this ground state responds to the symmetries of $SU(2)_L \times U(1)_Y$. If it was invariant, we would get:

$$e^{i\alpha\Lambda}\Phi_{ground} = \Phi_{ground} \Rightarrow \Lambda\Phi_{ground} = 0 \tag{2.63}$$

where Λ is one of the generators of $SU(2)_L \times U(1)_Y$, namely $\Lambda = T^{1,2,3}$ defined in

2.31 or $\Lambda = \frac{Y}{2} = \mathbb{1}$. However, we have:

$$\begin{aligned} T^1\Phi_{ground} &= \frac{1}{2}\begin{pmatrix}0 & 1\\ 1 & 0\end{pmatrix}\begin{pmatrix}0\\ v/\sqrt{2}\end{pmatrix} = \frac{1}{2}\begin{pmatrix}v/\sqrt{2}\\ 0\end{pmatrix} \neq 0 \\ T^2\Phi_{ground} &= \frac{1}{2}\begin{pmatrix}0 & -i\\ i & 0\end{pmatrix}\begin{pmatrix}0\\ v/\sqrt{2}\end{pmatrix} = \frac{-i}{2}\begin{pmatrix}v/\sqrt{2}\\ 0\end{pmatrix} \neq 0 \\ T^3\Phi_{ground} &= \frac{1}{2}\begin{pmatrix}1 & 0\\ 0 & -1\end{pmatrix}\begin{pmatrix}0\\ v/\sqrt{2}\end{pmatrix} = -\frac{1}{2}\begin{pmatrix}0\\ v/\sqrt{2}\end{pmatrix} \neq 0 \\ \frac{Y}{2}\Phi_{ground} &= \frac{1}{2}\begin{pmatrix}1 & 0\\ 0 & 1\end{pmatrix}\begin{pmatrix}0\\ v/\sqrt{2}\end{pmatrix} = \frac{1}{2}\begin{pmatrix}0\\ v/\sqrt{2}\end{pmatrix} \neq 0 \end{aligned} \tag{2.64}$$

The ground state does not respect any of these symmetries. But we can find one symmetry that is still there. We know from 2.39 that the electric charge Q can be written as $Q = T^3 + Y/2$. We can operate Φ_{ground} by Q:

$$Q\Phi_{ground} = (T^3 + \frac{Y}{2})\Phi_{ground} = \frac{1}{2}\left[\begin{pmatrix}1 & 0\\ 0 & -1\end{pmatrix} + \begin{pmatrix}1 & 0\\ 0 & 1\end{pmatrix}\right]\begin{pmatrix}0\\ v/\sqrt{2}\end{pmatrix} = 0 \tag{2.65}$$

This symmetry, denoted as $U(1)_{em}$ is therefore still a symmetry of the Lagrangian around this minimum. Hence we have broken three generators out of the original four. According to Goldstone's theorem, this corresponds to three massless particles.

2.5.3 Gauge boson masses and the Higgs boson

Next, we want to perturb the field around the minimum.

$$\Phi = \frac{1}{\sqrt{2}}\begin{pmatrix}\phi_1(x) + i\phi_2(x)\\ v + h(x) + i\phi_3(x)\end{pmatrix} \tag{2.66}$$

The Lagrangian must still be gauge invariant so we may simplify this by moving to the unitary gauge:

$$\Phi = \frac{1}{\sqrt{2}}\begin{pmatrix}0\\ v + h(x)\end{pmatrix} \tag{2.67}$$

This field can now be inserted to the Lagrangian 2.58. We begin with the first term of the Lagrangian and operate the field with the electroweak covariant derivative 2.40:

$$\begin{aligned} D_\mu\Phi &= \frac{1}{\sqrt{2}}\begin{pmatrix}\partial_\mu + \frac{ig}{2}\mathrm{W}^3_\mu + \frac{ig'}{2}\mathrm{B}_\mu & \frac{ig}{2}(\mathrm{W}^1_\mu - i\mathrm{W}^2_\mu)\\ \frac{ig}{2}(\mathrm{W}^1_\mu + i\mathrm{W}^2_\mu) & \partial_\mu - \frac{ig}{2}\mathrm{W}^3_\mu + \frac{ig'}{2}\mathrm{B}_\mu\end{pmatrix}\begin{pmatrix}0\\ v + h\end{pmatrix} \\ &= \frac{1}{\sqrt{2}}\begin{pmatrix}\frac{ig}{2}(\mathrm{W}^1_\mu - i\mathrm{W}^2_\mu)(v + h)\\ \partial_\mu h - i(v + h)(\frac{g}{2}\mathrm{W}^3_\mu - \frac{g'}{2}\mathrm{B}_\mu)\end{pmatrix} \end{aligned} \tag{2.68}$$

$$(D_\mu\Phi)^\dagger = \frac{1}{\sqrt{2}}\left(-\tfrac{ig}{2}(\mathrm{W}^1_\mu + i\mathrm{W}^2_\mu)(v + h),\quad \left(\partial_\mu h + i(v + h)(\tfrac{g}{2}\mathrm{W}^3_\mu - \tfrac{g'}{2}\mathrm{B}_\mu)\right)\right) \tag{2.69}$$

Using the fields for the physical particles 2.43 and 2.45 we obtain:

$$|D_\mu \Phi|^2 = \frac{1}{2}\partial_\mu h \partial^\mu h + \frac{1}{2}(v+h)^2\Big(\frac{g^2}{2}\mathrm{W}^-_\mu \mathrm{W}^{+\mu} + \frac{g^2+g'^2}{4}\mathrm{Z}_\mu \mathrm{Z}^\mu\Big) \tag{2.70}$$

Mass terms have appeared in the Lagrangian. The masses for $\mathrm{W}^\pm$ and Z can be read from the Lagrangian and are:

$$m_\mathrm{W} = \frac{vg}{2}, \quad m_\mathrm{Z} = \frac{v\sqrt{g^2+g'^2}}{2} \tag{2.71}$$

It's also worth noting that the photon is still massless. Also, the Weinberg angle introduced in 2.44 can be written as the ratio between the weak gauge boson masses:

$$\cos\theta_\mathrm{W} = \frac{m_\mathrm{W}}{m_\mathrm{Z}} \tag{2.72}$$

The potential part 2.59 of the scalar Lagrangian 2.58 is easy to calculate using the fact that $\Phi^\dagger\Phi = \frac{1}{2}(v+h)^2$ and that $\lambda = -(\frac{\mu}{v})^2$ (as defined in 2.61).

$$\begin{aligned} V(\Phi) = \mu^2\Phi^\dagger\Phi + \lambda(\Phi^\dagger\Phi)^2 &= \frac{1}{2}(v+h)^2(\mu^2 + \lambda\frac{1}{2}(v+h)^2) \\ &= \frac{1}{2}(v+h)^2(\mu^2 - \Big(\frac{\mu}{v}\Big)^2\frac{1}{2}(v+h)^2) \\ &= \frac{\mu^2 v^2}{2} - \mu^2 h^2 - \frac{\mu^2}{v}h^3 - \frac{\mu^2}{4v^2}h^4 \end{aligned} \tag{2.73}$$

The first term does not depend on any fields and therefore it does not affect the physics of the system and can be dropped. The entire Lagrangian is:

$$\begin{aligned} \mathcal{L}_{scalar} = &\frac{1}{2}\partial_\mu h \partial^\mu h + \frac{m^2_\mathrm{W}}{2}\mathrm{W}^+\mathrm{W}^- + \frac{m^2_\mathrm{Z}}{2}\mathrm{Z}^2 \\ &- \mu^2 h^2 + \frac{m^2_\mathrm{W}}{v}\mathrm{W}^+\mathrm{W}^- h + \frac{m^2_\mathrm{W}}{2v^2}\mathrm{W}^+\mathrm{W}^- h^2 \\ &+ \frac{m^2_\mathrm{Z}}{v}\mathrm{Z}^2 h + \frac{m^2_\mathrm{Z}}{2v^2}\mathrm{Z}^2 h^2 + \mu^2 v h^3 - \frac{\mu^2}{4v^2}h^4 \end{aligned} \tag{2.74}$$

We can identify the Higgs mass from the fourth term:

$$m_h = \sqrt{-2\mu^2} \tag{2.75}$$

The different interaction vertices between these particles are also predicted.

2.5.4 Yukawa couplings

So far, the fermions are all massless. The first idea to fix this would be to just add naive mass terms of the form

$$m(\psi_L^\dagger \psi_R + \psi_R^\dagger \psi_L) \tag{2.76}$$

However, this is not gauge invariant. The left-handed object transforms under $SU(2)$ but the right-handed one does not. Therefore we introduce *Yukawa couplings*.

$$\mathcal{L}_{Yuk} = -g_i(\bar{\psi_L}\Phi\psi_R + \bar{\psi_R}\Phi^\dagger\psi_L) \tag{2.77}$$

where ψ_L is a left-handed doublet and ψ_R is the corresponding singlet. This is gauge invariant having the two vector fields with a scalar field in the middle. As an example, let's use this to create the electron mass term.

$$\begin{aligned}\mathcal{L}_{Yuk} &= -g_e\left[\begin{pmatrix}\bar{\nu_{eL}} & \bar{e_L}\end{pmatrix}\begin{pmatrix}0\\ \frac{1}{\sqrt{2}}(v+h)\end{pmatrix}e_R + \bar{e_R}\begin{pmatrix}0, & \frac{1}{\sqrt{2}}(v+h)\end{pmatrix}\begin{pmatrix}\nu_{eL}\\ e_L\end{pmatrix}\right] \\ &= -\frac{1}{\sqrt{2}}g_e(v+h)[\bar{e_L}e_R + \bar{e_R}e_L] = -\frac{1}{\sqrt{2}}g_e(v+h)\bar{e}e\end{aligned} \tag{2.78}$$

This is indeed a mass term, letting us identify that

$$m_e = \frac{g_e(v+h)}{\sqrt{2}} \tag{2.79}$$

We see that the electron mass is proportional to the Yukawa coupling constant and the Higgs vacuum expectation value, as are all fermion masses in general. The Yukawa coupling, however, is different for each particle.

Since there currently are no right-handed neutrinos in the Standard Model, this mechanism cannot be used to create masses for the neutrinos, even though experimentally we know from neutrino oscillations that the masses must be nonzero.

2.6 Radiative corrections

If we wish to calculate the likelihood of some process with known initial and final states, the simplest approximation is to do it at tree level. In it we do not take into account Feynman diagrams with loops. This is what we did for example in Section 2.2.2 where we found the cross-section for an annihilation process at tree level. For more accuracy, higher orders should also be considered. These higher-order corrections are called *radiative corrections*. One example of a one-loop diagram can be seen in Figure 2.4. In principle all diagrams at any order should be taken into account. However, this is not possible to do in practise.

In addition to loops there are also other sources of higher order corrections. Processes may emit the so-called *bremsstrahlung* in the initial or final state. It is an extra photon which is emitted when a particle slows down and loses kinetic energy. There exist also the so called Faddeev-Popov ghost fields which don't correspond to any physical particles but are a necessary mathematical addition to preserve unitarity [30].

Usually the main contribution to the cross-section of a given process comes from lower order diagrams. The strength of the higher-order corrections depends on the coupling constant. We can do the corrections to a propagator, to a vertex or to a full interaction. These introduce corrections to the predicted physical quantities.

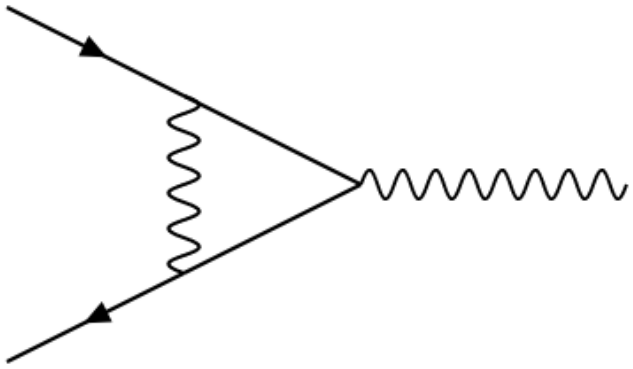

Figure 2.4: One possible one-loop diagram for an annihilation process into a photon. There are multiple higher-order diagrams for a given process and all of these affect the final results.

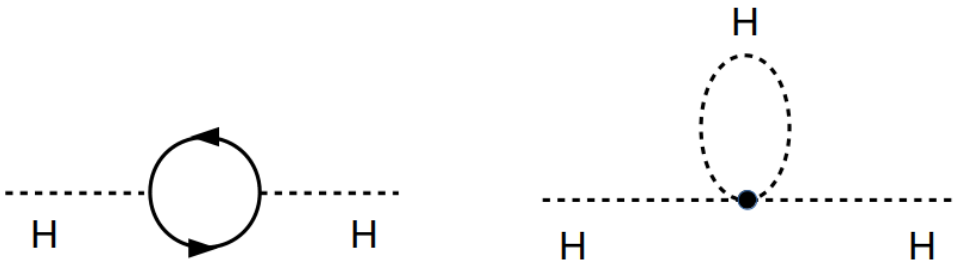

Figure 2.5: The 1-loop corrections to the Higgs boson mass via a fermion loop (left) and a Higgs boson loop (right).

As an example the corrections to a Higgs boson propagator change the prediction of its mass. In Image 2.5 we can see the two corrections to Higgs boson mass at 1-loop level. The contributions of these are summed to get a more accurate estimate on the Higgs boson mass.

In order to get finite answers from the integrals that arise, we need to use *cutoff regularization* where we instead of integrating to infinity use the *Planck scale* Λ as the upper limit. It is the scale where the quantum gravitational effects start to dominate and which we do not yet understand. Then the correction to the Higgs boson mass (Equation 2.75) at one-loop level is proportional to the square of the large cut-off:

$$\Delta m_{\mathrm{H}}^2 \approx -\frac{|g_{\mathrm{H}}^2|}{8\pi^2}\Lambda^2 \tag{2.80}$$

2.7 Problems and limitations of SM

The Standard Model has been an enormously successful theory. It has predicted for example the $W^{\pm}$ and Z bosons and the top quark before their detection.

However, SM has its shortcomings. Obviously it does not take into account gravity, but there are also more immediate questions. SM does not give explanation to the masses of the neutrinos which we experimentally know must exist due to neutrino oscillations [32]. It also does not give a particle candidate for dark matter, implied by astronomical observations [45]. The problem of baryon asymmetry, the fact that the universe consists almost entirely of matter instead of antimatter, is also left unexplained [45].

A non-ideal feature of the Standard Model is also the large number of free parameters in the theory. Without considering neutrino masses there are in total 18 free parameters: 6 quark masses, 3 lepton masses, the coupling constants g, g' and g_s, the Higgs potential parameters μ and λ, and finally the 4 independent parameters of the Cabibbo-Kobayashi-Maskawa (CKM) matrix which describes quark mixing. This is often seen as too much for a fundamental theory.

The *hierarchy problem* is related to the loop corrections for the Higgs boson mass. As seen in Equation 2.80, these corrections predict the Higgs boson mass being proportional to the square of the Planck scale. The Planck scale is 10^{29} GeV. Since we know the observed mass of the Higgs boson is 125 GeV, we need to adjust the Yukawa coupling coefficient g_{H} to be extremely small which seems rather mysterious and artificial.

These problems have been tackled by multiple theories such as string theory and supersymmetry. For example the Minimal Supersymmetric Standard Model contains among other things multiple Higgs bosons, two Higgs doublets to be exact. The models with two Higgs doublets are appropriately called *two-Higgs-doublet models*. These will be discussed in the following chapter.

3. Two-Higgs-doublet models

3.1 Theory of 2HDM

The Higgs sector in the current Standard Model is *minimal*, meaning it only contains one scalar doublet, the bare minimum for electroweak symmetry breaking. In two-Higgs-doublet models (2HDM) we introduce a non-minimal Higgs sector by adding an extra Higgs doublet.

$$\Phi_1 = \begin{pmatrix} \phi_1^+ \\ \phi_1^0 \end{pmatrix}, \ \Phi_2 = \begin{pmatrix} \phi_2^+ \\ \phi_2^0 \end{pmatrix} \tag{3.1}$$

There are some constraints these doublets must fulfil [51]. Let's define the parameter ρ as follows:

$$\rho \equiv \frac{m_{\mathrm{W}}^2}{m_{\mathrm{Z}}^2 \cos^2 \theta_{\mathrm{W}}} = \frac{\sum_{i=1}^{n} [T_i(T_i+1) - \frac{1}{4} Y_i^2] v_i}{\sum_{i=1}^{n} \frac{1}{2} Y_i^2 v_i} \tag{3.2}$$

Experimentally this parameter has been measured to be close to 1. It constrains $Y^2 = 1$. We will choose both Higgs doublets to have the hypercharge $Y = 1$. Since these are all complex fields and therefore have two independent components, there are now eight degrees of freedom.

3.1.1 The 2HDM potential

The most general gauge-invariant potential with two scalar Higgs doublets becomes [9]:

$$\begin{aligned} V = & m_{11}^2 \Phi_1^\dagger \Phi_1 + m_{22}^2 \Phi_2^\dagger \Phi_2 - m_{12}^2 \Phi_1^\dagger \Phi_2 + h.c. \\ & + \frac{\lambda_1}{2} (\Phi_1^\dagger \Phi_1)^2 + \frac{\lambda_2}{2} (\Phi_2^\dagger \Phi_2)^2 + \lambda_3 \Phi_1^\dagger \Phi_1 \Phi_2^\dagger \Phi_2 \\ & + \lambda_4 \Phi_1^\dagger \Phi_2 \Phi_2^\dagger \Phi_1 + \frac{1}{2} \lambda_5 (\Phi_1^\dagger \Phi_2)^2 + h.c. \\ & + \lambda_6 \Phi_1^\dagger \Phi_1 \Phi_1^\dagger \Phi_2 + h.c. + \lambda_7 \Phi_2^\dagger \Phi_2 \Phi_1^\dagger \Phi_2 + h.c. \end{aligned} \tag{3.3}$$

where *h.c.* stands for the Hermitian conjugate of the previous term. The potential is Hermitian from which it follows that the parameters $\lambda_{1,2,3,4}$ are real.

We can impose additional constraints to this general form. At tree level there are no *flavor changing neutral currents* (FCNC) in the SM. It is an interaction where the flavor of a quark is changed in a process mediated by a neutral boson, in the case of the SM the Z boson. Forbidding these interactions at tree-level in the Higgs

boson mediated case requires us to set $\lambda_6 = \lambda_7 = m_{12} = 0$. This corresponds to imposing a discrete symmetry $\Phi_1 = -\Phi_1$. For the purposes of this example, we will allow a small symmetry break by letting $m_{12} \neq 0$.

Some extra constraints can be added. We want the vacuum to be stable, i.e. there is no direction where the potential decreases without bound (or stays flat to infinity). With the conditions $\lambda_6 = \lambda_7 = 0$ this gives [33]:

$$\lambda_1 > 0, \quad \lambda_2 > 0, \quad \lambda_3 + \sqrt{\lambda_1 \lambda_2} > 0, \quad \lambda_3 + \lambda_4 \pm |\lambda_5| + \sqrt{\lambda_1 \lambda_2} > 0 \tag{3.4}$$

In general, these models can violate CP-symmetry [38]. Assuming that the Higgs sector does not violate CP-symmetry, minimizing the potential produces fields analogous with 2.62:

$$\Phi_1 = \frac{1}{\sqrt{2}} \begin{pmatrix} 0 \\ v_1 \end{pmatrix}, \quad \Phi_2 = \frac{1}{\sqrt{2}} \begin{pmatrix} 0 \\ v_2 \end{pmatrix} \tag{3.5}$$

In order to conserve the gauge boson masses obtained with the canonical Higgs mechanism, the parameters must fulfil

$$v^2 = v_1^2 + v_2^2 \tag{3.6}$$

Commonly a parameter β is introduced so that $v_1 = v \cos\beta$ and $v_2 = v \sin\beta$. This way the ratio between v_1 and v_2 can be expressed as

$$\tan\beta = \frac{v_2}{v_1} \tag{3.7}$$

Minimizing the potential at this minimum results in the following masses:

$$m_{11}^2 = m_{12}^2 \tan\beta - \frac{v^2}{2}(\lambda_1 \cos^2\beta + (\lambda_3 + \lambda_4 + \lambda_5)\sin^2\beta) \tag{3.8}$$

$$m_{22}^2 = m_{12}^2 \cot\beta - \frac{v^2}{2}(\lambda_2 \sin^2\beta + (\lambda_3 + \lambda_4 + \lambda_5)\cos^2\beta) \tag{3.9}$$

3.1.2 The Higgs sector in 2HDM

Next, following what we did in Section 2.5.3, we perturb these fields around the minimum and obtain eight independent fields:

$$\Phi_n = \begin{pmatrix} \phi_n^+ \\ \frac{1}{\sqrt{2}}(v_n + \rho_n + \eta_n) \end{pmatrix}, \quad n = 1, 2 \tag{3.10}$$

Three of these are massless Goldstone bosons that get "eaten" by the $W^\pm$ and Z fields like in the one-Higgs boson case. But now there are five extra fields, so we get five Higgs bosons in total. There are two charged scalars, two neutral scalars (scalars are even under CP symmetry) and one neutral pseudoscalar (CP-odd). Using the potential 3.3 the mass terms for the charged bosons corresponding to ϕ_n^+ and $\phi_n^- = (\phi_n^+)^\dagger$ can be written as:

$$\mathcal{L}_{m(\phi^\pm)} = [m_{12}^2 - (\lambda_4 + \lambda_5)v_1 v_2] \begin{pmatrix} \phi_1^-, & \phi_2^- \end{pmatrix} \begin{pmatrix} \frac{v_2}{v_1} & -1 \\ -1 & \frac{v_1}{v_2} \end{pmatrix} \begin{pmatrix} \phi_1^+ \\ \phi_2^+ \end{pmatrix} \tag{3.11}$$

To find the masses of the physical particles, we must move to mass basis by diagonalizing the matrix.

$$\frac{1}{v_1 v_2}\begin{pmatrix} v_2^2 & -v_1 v_2 \\ -v_1 v_2 & v_1^2 \end{pmatrix} = \frac{1}{v_1 v_2}\begin{pmatrix} \frac{v_1}{v} & -\frac{v_2}{v} \\ \frac{v_2}{v} & \frac{v_1}{v} \end{pmatrix}\begin{pmatrix} 0 & 0 \\ 0 & v^2 \end{pmatrix}\begin{pmatrix} \frac{v_1}{v} & \frac{v_2}{v} \\ -\frac{v_2}{v} & \frac{v_1}{v} \end{pmatrix} \tag{3.12}$$

From this the combinations corresponding to the mass eigenstates (Goldstone bosons and charged Higgs bosons) can be found.

$$\begin{aligned}\begin{pmatrix} \frac{v_1}{v} & \frac{v_2}{v} \\ -\frac{v_2}{v} & \frac{v_1}{v} \end{pmatrix}\begin{pmatrix} \phi_1^+ \\ \phi_2^+ \end{pmatrix} &= \begin{pmatrix} \cos\beta & \sin\beta \\ -\sin\beta & \cos\beta \end{pmatrix}\begin{pmatrix} \phi_1^+ \\ \phi_2^+ \end{pmatrix} \\ &= \begin{pmatrix} \phi_1^+\cos\beta + \phi_2^+\sin\beta \\ -\phi_1^+\sin\beta + \phi_2^+\cos\beta \end{pmatrix} \equiv \begin{pmatrix} \mathrm{G}^+ \\ \mathrm{H}^+ \end{pmatrix}\end{aligned} \tag{3.13}$$

Here one can read that the boson H^+ is characterised by the mixing angle β:

$$\mathrm{H}^+ = -\phi_1^+\sin\beta + \phi_2^+\cos\beta \tag{3.14}$$

So in this basis the mass Lagrangian is

$$\mathcal{L}_{m(\phi^\pm)} = v^2[m_{12}^2 - (\lambda_4+\lambda_5)v_1 v_2]\begin{pmatrix} \mathrm{G}^-, & \mathrm{H}^- \end{pmatrix}\begin{pmatrix} 0 & 0 \\ 0 & 1 \end{pmatrix}\begin{pmatrix} \mathrm{G}^+ \\ \mathrm{H}^+ \end{pmatrix} \tag{3.15}$$

The Goldstone bosons are clearly massless, whereas the masses of the charged Higgs bosons are

$$m_{\mathrm{H}^\pm}^2 = \Big[\frac{m_{12}^2}{v_1 v_2} - (\lambda_4+\lambda_5)\Big](v_1^2+v_2^2) \tag{3.16}$$

The mass term Lagrangian for the pseudoscalar is:

$$\mathcal{L}_{m(\eta)} = \Big[\frac{m_{12}^2}{v_1 v_2} - 2\lambda_5\Big]\begin{pmatrix} \eta_1, & \eta_2 \end{pmatrix}\begin{pmatrix} v_2^2 & -v_1 v_2 \\ -v_1 v_2 & v_1^2 \end{pmatrix}\begin{pmatrix} \eta_1 \\ \eta_2 \end{pmatrix} \tag{3.17}$$

Here we get one massless Goldstone boson and one massive CP-odd scalar. The pseudoscalar is denoted by A^0. Its mass becomes

$$m_{\mathrm{A}}^2 = \Big[\frac{m_{12}^2}{v_1 v_2} - 2\lambda_5\Big](v_1^2+v_2^2) \tag{3.18}$$

and the mixing is again characterised by the angle β:

$$\mathrm{A} = -\sqrt{2}\,\mathrm{Im}(\phi_1^0)\sin\beta + \sqrt{2}\,\mathrm{Im}(\phi_2^0)\cos\beta \tag{3.19}$$

The case of the CP-even scalars is a bit more complicated.

$$\mathcal{L}_{m(\rho)} = -\begin{pmatrix} \rho_1, & \rho_2 \end{pmatrix} M \begin{pmatrix} \rho_1 \\ \rho_2 \end{pmatrix} \tag{3.20}$$

where the matrix M is

$$M = \begin{pmatrix} m_{12}^2\frac{v_2}{v_1} + \lambda_1 v_1^2 & -m_{12}^2 + (\lambda_3+\lambda_4+\lambda_5)v_1 v_2 \\ -m_{12}^2 + (\lambda_3+\lambda_4+\lambda_5)v_1 v_2 & m_{12}^2\frac{v_1}{v_2} + \lambda_2 v_2^2 \end{pmatrix} \tag{3.21}$$

It turns out that when diagonalizing this matrix, a massless state does not appear. Instead, we get two massive Higgs bosons, denoted by h^0 and H^0. Their masses can be expressed using the elements of the matrix M.

$$m_{\mathrm{H}^0,\mathrm{h}^0} = M_{11} + M_{22} \pm \sqrt{(M_{11} - M_{22})^2 + 4M_{12}^2} \tag{3.22}$$

We can see that their masses differ. The bosons are defined so that H^0 is heavier than h^0. The mixing angle is now a new angle, denoted as α:

$$\mathrm{h}^0 = -(\sqrt{2}\,\mathrm{Re}(\phi_1^0) - v_1)\sin\alpha + (\sqrt{2}\,\mathrm{Re}(\phi_2^0) - v_2)\cos\alpha \tag{3.23}$$

$$\mathrm{H}^0 = (\sqrt{2}\,\mathrm{Re}(\phi_1^0) - v_1)\cos\alpha + (\sqrt{2}\,\mathrm{Re}(\phi_2^0) - v_2)\sin\alpha \tag{3.24}$$

Now we have found all five Higgs bosons of 2HDM: the charged scalars $\mathrm{H}^\pm$, the neutral pseudoscalar A and the neutral scalars h^0 and H^0.

There exist different versions of the two-Higgs-doublet model. Most notably there are Type I and Type II 2HDMs. They differ in the way the two Higgs doublets couple to fermions. In Type I 2HDM all charged leptons and quarks couple to the second Higgs doublet Φ_2 whereas in the Type II 2HDM down-type quarks and charged leptons couple to Φ_1 and up-type quarks couple to Φ_2. In this study we shall focus on the Type II 2HDM since the chosen final state is sensitive to only Type II 2HDM, which includes the Minimal Supersymmetric Standard Model as a special case.

In 2HDM fermion masses can again be created through Yukawa couplings similar to 2.77. The only difference is that now the couplings to the Higgs boson are modified by factors relating to the two mixing angles α and β.

3.2 Properties of charged Higgs bosons

The predominant production process of the charged Higgs boson depends on its mass. If the charged Higgs mass is smaller than the mass difference between the top and bottom quarks ($m_{\mathrm{H}^\pm} < m_\mathrm{t} - m_\mathrm{b} \approx 169\,\mathrm{GeV}$), it is called a *light* charged Higgs boson. Conversely, if $m_{\mathrm{H}^\pm} > m_\mathrm{t} - m_\mathrm{b}$, it is called a *heavy* charged Higgs boson.

For the light charged Higgs boson the dominant production is a decay of a top quark into the charged Higgs boson and a bottom quark (Figure 3.1), which clearly is not possible any more when the Higgs boson is heavy.

For the heavy boson the direct production can be calculated in different schemes. In the *four-flavor scheme* (4FS) no bottom quarks are present in the initial state, unlike in the *five-flavor scheme* (5FS). When calculated to the lowest order, the cross-sections from these two methods differ significantly, while in the next-to-lowest order the differences are already much smaller [27]. In infinite order the results of these two approaches agree exactly since the only difference is how the perturbation theory is ordered. In the five-flavor scheme there indeed is a bottom quark in the initial state of the dominant process which is shown in Figure 3.2.

The difference between the 4FS and the 5FS is formally logarithmic. The 4FS and the 5FS provide unique descriptions of the cross sections in the limits $\ln(m(\mathrm{H}^\pm)/m(\mathrm{b})) \to 2$ (for the 4FS) and $\ln(m(\mathrm{H}^\pm)/m(\mathrm{b})) \to \infty$ (for the 5FS).

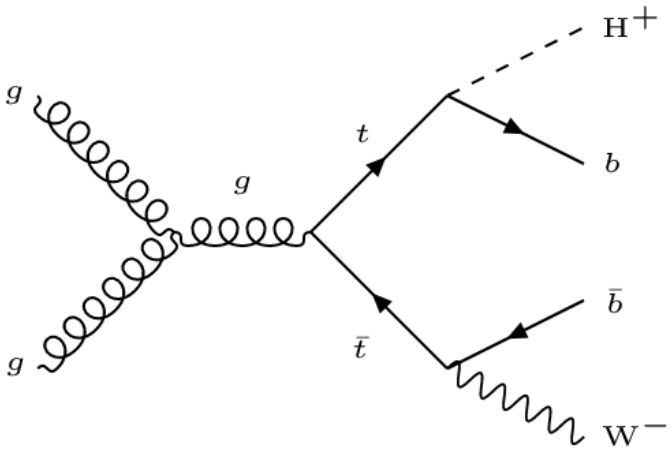

Figure 3.1: The dominant production mechanism for the light charged Higgs boson: a decay of a top quark. In all diagrams the diagram for H^- can be obtained by charge-conjugation.

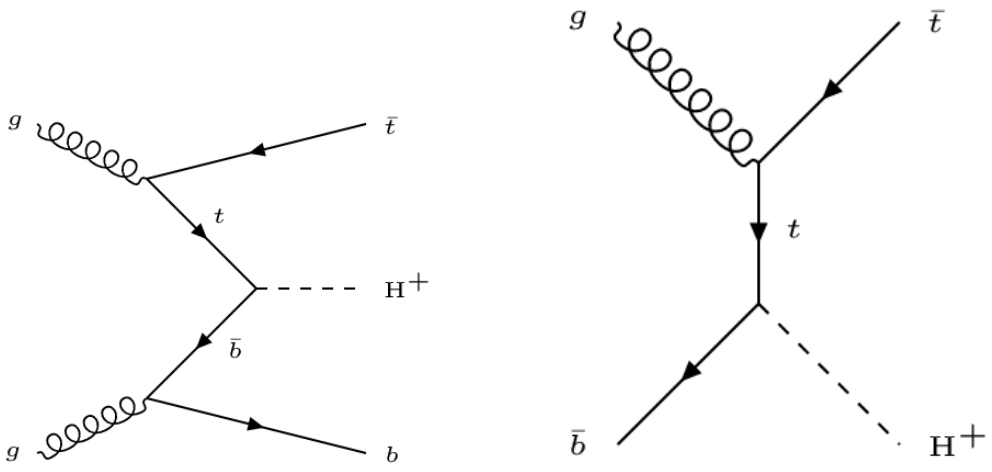

Figure 3.2: The dominant production mechanisms for the heavy charged Higgs boson in the 4FS (left) and the 5FS (right). The processes are the same, but in the 5FS the bottom quark is defined as the initial state.

The two schemes are combined with a weight that depends logarithmically on $m(\mathrm{H}^{\pm})/m(\mathrm{b})$. The combination scheme is called the *Santander matching scheme* [35]. It is defined as:

$$\sigma_{matched} = \frac{\sigma_{4FS} + w\sigma_{5FS}}{1 + w} \tag{3.25}$$

where the weight w is:

$$w = \ln(m(\mathrm{H}^{\pm})/m(\mathrm{b})) - 2 \tag{3.26}$$

The dominant decay mode of the charged Higgs boson depends on its mass as well as the couplings between $\mathrm{H}^{\pm}$ and its decay products. Also, in the Minimal Supersymmetric Standard Model the Type II 2HDM calculations get modifications from effects caused by the supersymmetric particles. In Figure 3.3 the Minimal Supersymmetric Standard Model branching fractions for one benchmark scenario (m_{h}^{mod-}) [12] are shown with two values of $\tan\beta$.

From Figure 3.3 we can see that when the charged Higgs boson is light, the dominant process is $\mathrm{H}^{\pm} \to \tau\nu$, at least with the chosen values of $\tan\beta$. However, when the boson is heavier than 200 GeV, the decay $\mathrm{H}^{\pm} \to$tb is more probable. The decays to cs and $\mu\nu$ are also possible. Some decays into supersymmetric particles may also happen, although they are not pictured.

While it is clear from these plots that for the light charged Higgs boson the $\tau\nu$ channel is attractive, it can be useful also for the heavy Higgs search. Firstly, the proportion of this channel grows as $\tan\beta$ grows so with large values of this parameter this decay may be very common. There are also experimental reasons that make it easier to extract this signal from the Standard Model background.

3.3 The Minimal Supersymmetric Standard Model

In supersymmetry every particle has a supersymmetric partner which has a spin differing one half from the original. Therefore the superpartner of a fermion is a boson and the superpartner of a boson is a fermion. If the supersymmetry was perfect, each superpartner, known as a "sparticle", would have the same quantum numbers as their partners apart from spin. They would also have equal masses. Since no sparticles have been found yet, the symmetry must be broken and the sparticles must have much higher masses than their regular counterparts [31].

No experimental evidence for supersymmetry has been found to date but it does have some appealing properties. It would solve the hierarchy problem since it turns out that the contributions from superpartners would cancel out the divergent terms in the SM particle loop expansions [6]. It also nicely unifies the weak, electromagnetic and strong interactions at high energy scales. There is also a possibility of a sparticle being the mysterious constituent of the dark matter. For this a viable candidate is the neutralino [39].

The Minimal Supersymmetric Standard Model (MSSM) adds the minimum amount of new particles and interactions to the Standard Model [50]. It requires two Higgs fields and is a Type II 2HDM. It also adds extra constraints to the 2HDM. Only two free parameters are needed to describe the MSSM Higgs sector at

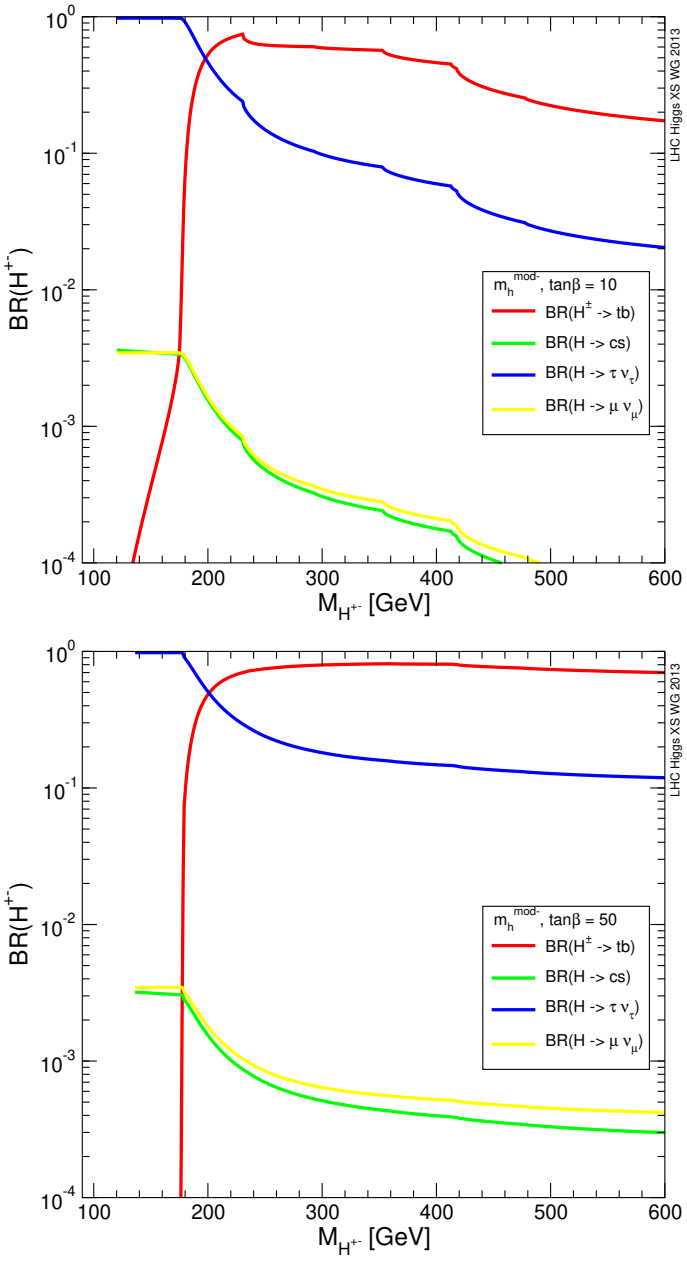

Figure 3.3: The branching fractions of $H^{\pm}$ with $\tan\beta = 10$ and $\tan\beta = 50$. This is from the Minimal Supersymmetric Standard Model m_h^{mod-} benchmark scenario. The image is taken from [13].

tree level [28]. These can be chosen as m_{A} and $\tan\beta$. However, radiative corrections from higher orders might by quite large.

The MSSM has a lot of free parameters. Therefore different *benchmark scenarios* have been created. These scenarios cover a wide range of parameter values showcasing different phenomenological properties. One category of these are the m_h^{mod} scenarios (used for example in Fig 3.3). where the observed Higgs boson corresponds to the lighter CP-even Higgs boson for a wide range of $\tan\beta$ values [12].

As noted in the previous chapter regarding the 2HDM, there are new possibilities of CP-violation in the MSSM. It raises the question that if supersymmetry exists, why do we observe so little CP-violation in nature.

4. The Large Hadron Collider and the CMS Experiment

4.1 The Large Hadron Collider

The Large Hadron Collider (LHC) is the largest and most powerful particle accelerator in the world. It's a circular collider with a circumference of 26.7 km situated near the city of Geneva at the border between France and Switzerland. It was built in early 2000s in an existing tunnel previously occupied by the Large Electron-Positron Collider (LEP). As the name suggests, LHC collides hadrons. This study will focus on proton-proton collisions, but the LHC is also used for heavy ion collisions. The technical aspects of the LHC are detailed in [10].

Two proton beams circulate the LHC in opposite directions. They are set to collide at 4 interaction points around the ring. The main detectors at these interaction points are ALICE (A Large Ion Collider Experiment), ATLAS (A Toroidal LHC ApparatuS) CMS (Compact Muon Solenoid), and LHCb (Large Hadron Collider beauty). Of these, ATLAS [1] and CMS [14] were the ones that found the Higgs boson in 2012.

The protons in the LHC are accelerated using electric fields and guided by magnetic fields. An important variable in assessing the strength of the collider is the *center-of-mass energy* $\sqrt{s}$ where $s = (p_1 + p_2)^2$. For most processes of interest their production rate grows as $\sqrt{s}$ grows, which is why maximising its value is desirable. For LHC Run2, data recorded between 2015 and 2018 the center-of-mass energy was $\sqrt{s} = 13$ TeV. Currently LHC is on its second *long shutdown* and it is designed to be reopened in Autumn 2021.

Protons must be pre-accelerated before they enter the LHC pipe. Their journey begins from a bottle of hydrogen where the hydrogen atoms are ionized. The protons are firstly accelerated with a linear accelerator (LINAC) up to an energy of 50 MeV (a speed of 0.3c). From there the protons are accelerated in the Proton Synchrotron Booster, the Proton Synchrotron (PS) and the Super Proton Synchrotron (SPS) until they are finally ready for the LHC. When the protons enter the LHC they have an energy of 450 GeV from which they are accelerated to the final energy of 6.5 TeV. This corresponds to a velocity of $(1 - 10^{-8})c$.

The LHC beam consists of *bunches* of protons. Each bunch contains approximately 1.15×10^{11} protons. For LHC Run 2 the bunch spacing was 25 ns which corresponds to a frequency of 40 MHz. However, most of the protons do not collide

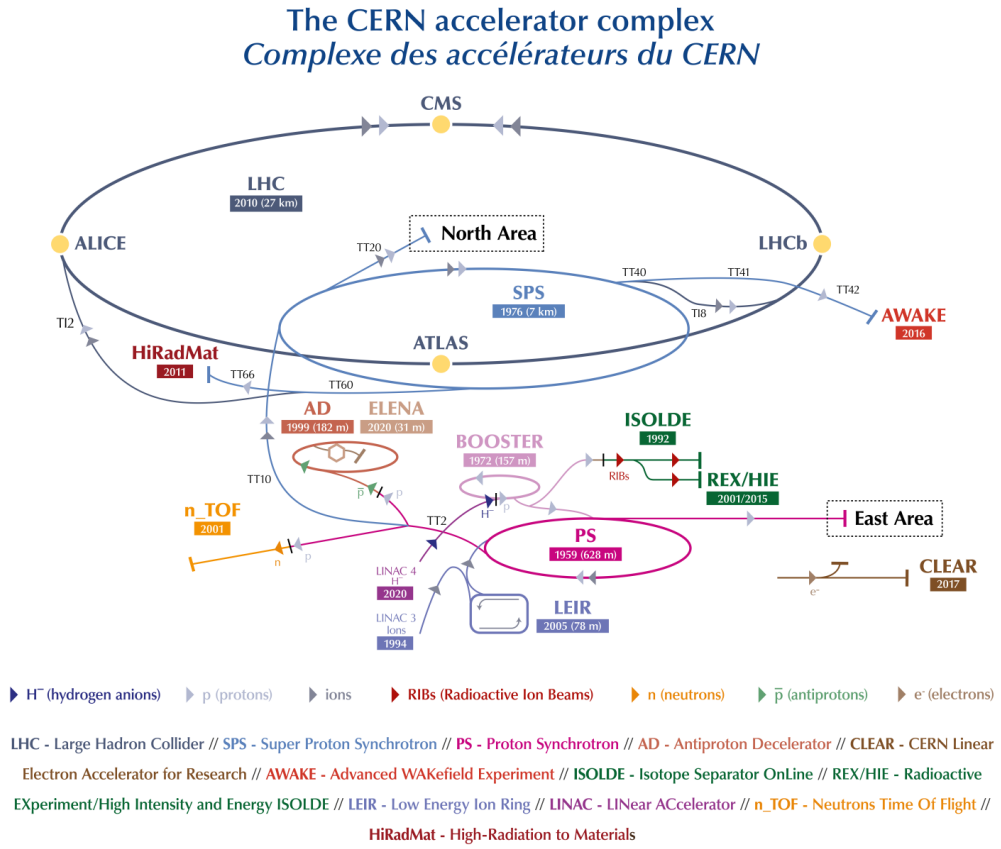

Figure 4.1: A diagram of the accelerator complex at CERN. Among others, all accelerators used to accelerate protons for the LHC can be seen as well as the locations of the 4 main detectors along the LHC. [41]

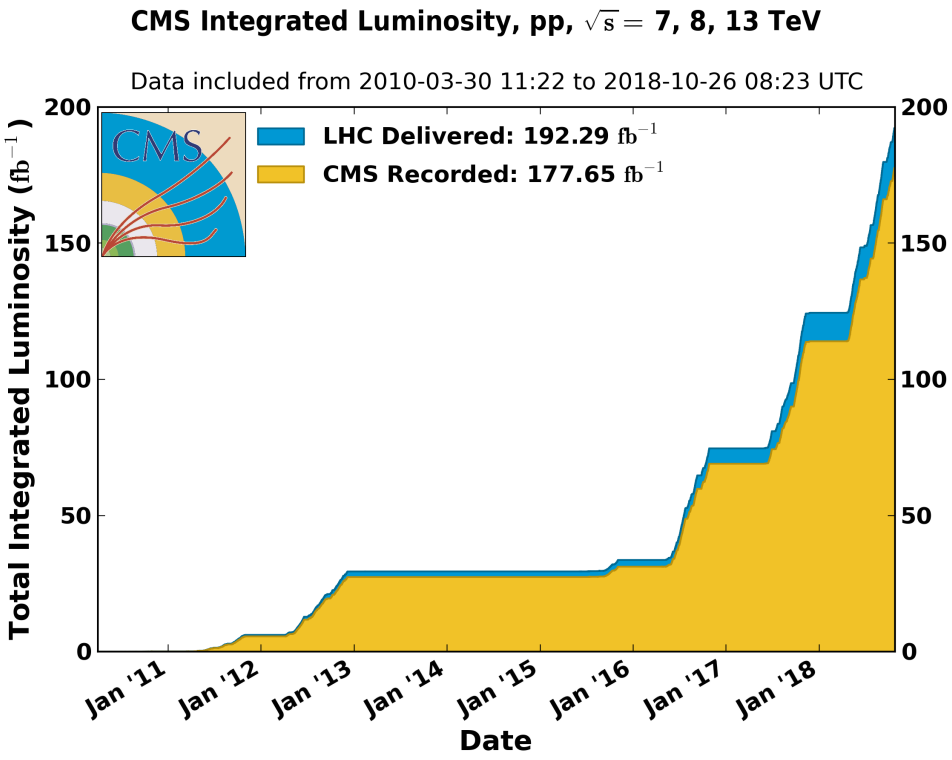

Figure 4.2: The overall integrated luminosity of the CMS experiment. The first long shutdown in 2013-2015 can be clearly seen. During it many upgrades were made which resulted in a sharp growth of the collected integrated luminosity. [17]

in bunch crossings. The average number of interactions in one bunch crossing is called the *pileup*. At the end of Run 2, the average pileup of CMS was approximately 40, meaning on average 40 simultaneous collisions happen in every bunch crossing.

Instantaneous luminosity $\mathcal{L}$ is the ratio between the production rate of a process dN/dt and the cross section of the process:

$$\mathcal{L} = \frac{1}{\sigma}\frac{dN}{dt} \tag{4.1}$$

Integrating over it produces the *integrated luminosity* L which is proportional to N, the amount of collected data.

$$N = \sigma \int_0^T \mathcal{L} dt = \sigma L \tag{4.2}$$

Most of the collected integrated luminosity is from the latest Run as is evident in Fig. 4.2. The planned *High Luminosity LHC* aims to multiply the integrated luminosity by a factor of 10 [7].

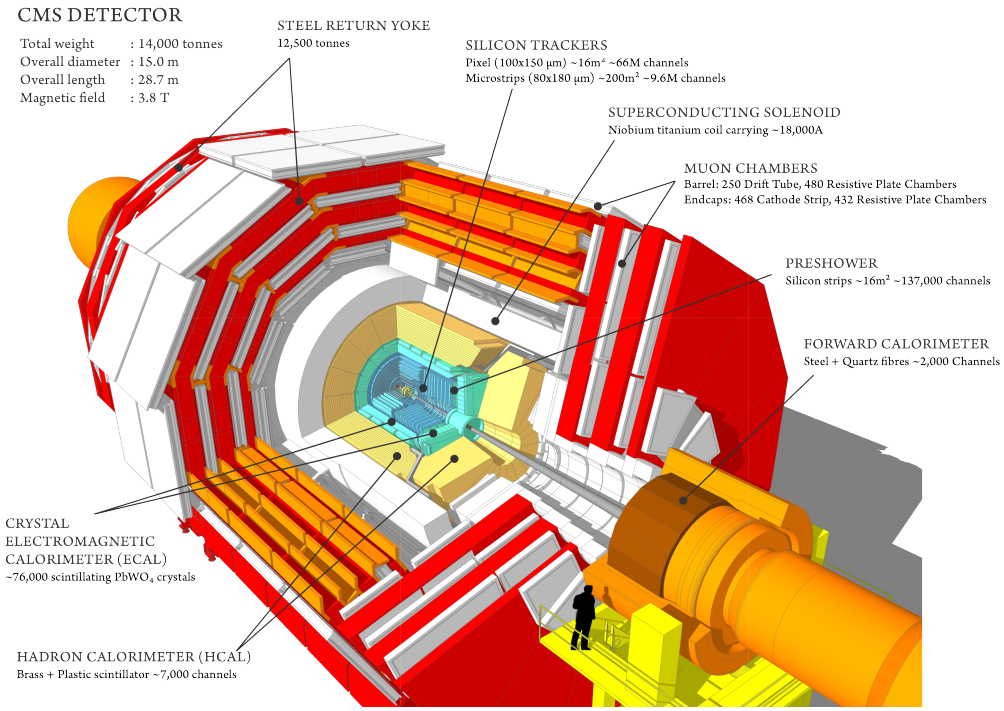

Figure 4.3: An opened view into the CMS detector. [44]

4.2 The Compact Muon Solenoid experiment

The Compact Muon Solenoid (CMS) experiment is located in the village of Cessy in France, 100 meters underground. It is called *compact*, since while it weights 14,000 tonnes, it is only 25 meters long and 15 meters in diameter, making it heavier but significantly smaller than ATLAS. While CMS is a general-purpose detector, detecting all sorts of particles in proton-proton as well as heavy ion collisions, its most distinct feature are the large muon chambers on the outer rim. Inside those there is a superconducting solenoid magnet, giving the final letter for the abbreviation. The CMS detector consists of different *sub-detectors*, which are designed to detect different particles. They are layered around the collision point, as seen in Figures 4.3 and 4.4. A more thorough explanation can be found in Ref [19].

4.2.1 Tracking system

The goal of the inner tracking system is to measure the trajectories of the outgoing particles at high precision. It has a cylindrical shape with a length of 5.8 m and a diameter of 2.6 m. The silicon *pixel tracker* is located closest to the detector, with small pixels of size 100×150 μm providing extra accuracy. Rest of the tracking system consists of larger *silicon strips*.

Because of the intense particle flux near the interaction point the pixel detector needs to be highly resistant to radiation damage. Due to the high luminosity a fast response time for the trackers is also needed. Both trackers are based on ionization in a semiconductor pn-junction, creating an electric current which is collected and

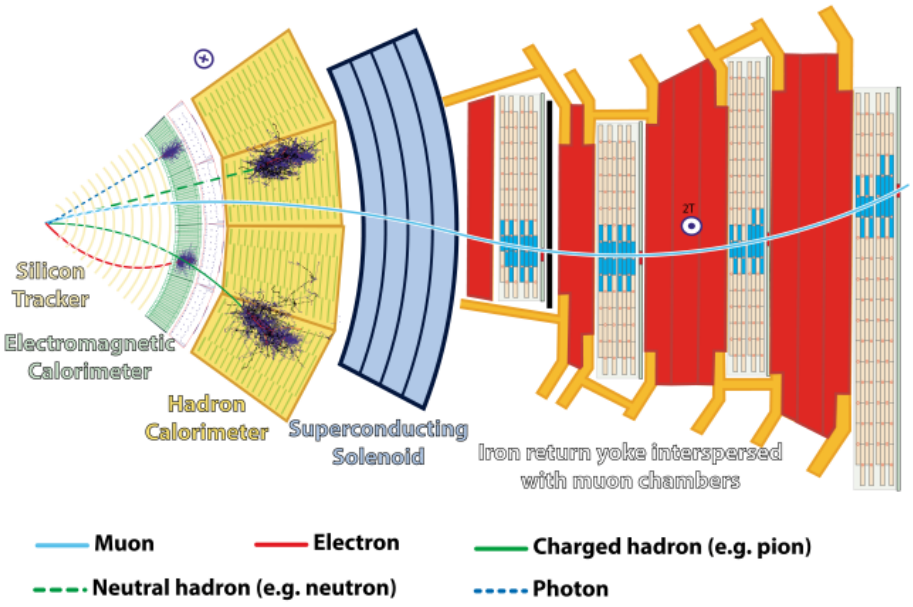

Figure 4.4: A slice of the CMS detector. One can see how electrons and photons stop at ECAL, while hadrons continue to HCAL and muons travel all the way to the outside muon chambers. [8]

measured at the electrodes. The measurement of the trajectories is important for reconstructing *primary* and *secondary vertices* and for determining the transverse momenta. The primary vertices are reconstructed from tracks coming from proton-proton collisions and the secondary vertices are created when a particle decays.

4.2.2 Electromagnetic calorimeter

Next layer after the tracking systems is the electromagnetic calorimeter (ECAL). It is made of one layer of lead tungstate ($PbWO_4$) crystals. It is a very dense material with a density of 8.3 g/cm^3. This means that one layer (22-23 cm) of lead tungstate is enough to stop electrons with a very high probability. This can be quantified with a *radiation length* which is the mean distance where an electron loses $1/e$ of its energy. The radius of the ECAL corresponds to approximately 25 radiation lengths.

The energy of a stopped particle can be collected and measured from the energy of scintillation light from the lead tungstate crystals. A favorable probability of lead tungstate is also its short excitation time, most scintillation light is emitted within 25 ns. Hadrons also lose some of their energy in the ECAL. An *interaction length* describes the average distance a particle can travel before inelastically hitting a nucleus. For hadrons, the interaction length in the ECAL is approximately equal to the size of the ECAL. Therefore many hadrons lose their energy already in the ECAL.

4.2.3 Hadronic calorimeter

The hadronic calorimeter (HCAL) is designed to stop rest of the particles with the exception of muons that are measured in the muon chambers and neutrinos or other

very weakly interacting particles that cannot be caught. The HCAL is comprised of alternating layers of passive brass absorber and active plastic scintillator material. The hadrons collide with nuclei in the passive layers creating so called *hadronic showers* consisting of secondary particles. This creates scintillation light in the active layer, which is then measured by photodetectors. Since part of the energy is absorbed by the passive layer, the energy must be estimated indirectly from active layer data. ECAL data is also used for the hadrons that already begin their shower there.

4.2.4 Muon chambers

The muon chambers are located outside the solenoid magnet. They are interleaved with steel plates of magnetic *return yoke* which contains and guides the magnetic field. The chambers consist of three different types of gaseous particle detectors. The barrel part contains four layers of aluminum *drift tubes* (DT) while the ends, called *endcaps*, use *cathode strip chambers* (CSC). Both DTs and CSCs are complemented with *resistive plate chambers* (RPC).

The drift tubes are filled with ionizable gas (85% argon, 15% carbon dioxide) with a positively charged wire in the middle of each tube. A muon traversing the tube ionizes the gas creating secondary electrons which drift in the tube towards the wire's positive charge. The electrons also ionize more electrons on the way, creating an avalanche. Hitting the wire creates an electric signal which is then measured. The drift time is typically in the order of 100 ns.

In the endcaps the muon and the background rates are high and the magnetic field is large and non-uniform. The cathode strip chambers work in a similar manner to the drift tubes. The main difference is that they contain a large number of alternating negatively charged cathode strips and positively charged anode wires. The gas mixture they use is 40% argon, 50% carbon dioxide and 10% carbon tetrafluoride (CF_4).

Since the eventual background rates and the ability of the muon chambers to measure beam-crossing time were uncertain, a complementary trigger system of resistive plate chambers was added. In the RPCs the gas is sandwiched between two resistive plates which are coated with graphite. They produce a fast response with good time resolution but worse spatial resolution compared to the DTs and the CSCs.

4.2.5 The CMS coordinate system

In the CMS a specific coordinate system is used, shown in Fig 4.5. The origin corresponds to the nominal interaction point in the middle of the detector. The direction along the beam pipe is denoted by the coordinate z. The positive z-axis points to the direction of the anticlockwise beam. The angle ϕ parametrizes the angle perpendicular to the beam pipe and spans the angle $[0, 2\pi]$. The polar angle θ is measured with respect to the positive z-axis and spans the angle $[0, \pi]$. In practise,

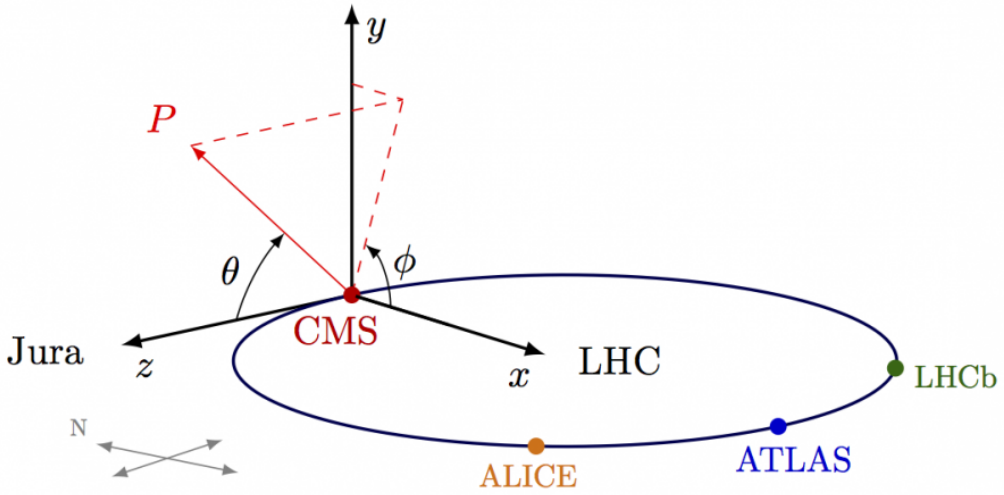

Figure 4.5: The coordinate system used at the CMS. [43]

instead of θ, a quantity called *pseudorapidity* is used instead. It is defined as

$$\eta = -\ln(\tan(\frac{\theta}{2})) \tag{4.3}$$

This means that η takes values from $-\infty$ to ∞ with the absolute value getting larger towards the z-axis and $\eta = 0$ defining the transverse plane.

4.3 Reconstruction of CMS events

The event reconstruction of the CMS events is based on the Particle Flow algorithm (PF) [24]. It uses a deterministic annealing algorithm. It first reconstructs individual particle candidates: muons, electrons, photons, charged and neutral hadrons. More complicated objects, such as tau jets, are built from those. The vertex with the highest transverse momentum tracks is considered the primary vertex of the hard interaction. Muons, electrons, and hadronically decaying tau leptons are required to originate from this primary vertex.

Electrons are reconstructed combining their energy deposits in the ECAL and hits in the silicon tracker. Additionally, electrons must pass some identification requirements. These are based on the cluster shapes, the amount of energy deposited in the HCAL and the direction of the tracks.

For muons the tracks from the silicon tracker are combined with individual hits or tracks reconstructed in the muon detection system. Again, some selection criteria are applied.

Jets are reconstructed from particle flow candidates using a clustering algorithm. The origin of the jets also needs to be identified. The jets originating from bottom quarks (known as *b jets*) can be recognized using a *b tagging algorithm*.

Hadronic tau leptons are reconstructed using the hadrons-plus-strips algorithm [22]. It needs to separate the tau jets from the quark and gluon jets as well as from the electrons and muons. The algorithm examines the candidates that are

seeded by jets and consist of either one neutral pion and up to two charged pions or three charged pions. The neutral pions decay quickly into two photons. They are reconstructed as strips of electromagnetic particles.

Individual neutrinos are impossible to detect directly. However, there is a way to determine whether an event has emitted a neutrino. In the collision the transverse energy of the event is zero and this quantity is conserved. Therefore we may find the energy of the neutrino by the *missing transverse energy* (MET).

5. CMS trigger system

During Run 2 data taking the proton beams collided once every 25 nanoseconds. This means 40,000,000 collisions per second. The pileup raises the count of individual proton-proton collisions by an additional factor of 40. The result is that not all data collected by the CMS can be saved due to limiting writing speed. The data is filtered by the so-called *triggers*. The goal is to pick the interesting events out to further analysis. This needs to be done quickly and computationally efficiently.

The triggering system is divided into two parts: the Level 1 trigger (L1) and the High-level Trigger (HLT). The output rate is reduced from 40 GHz firstly to 100 kHz in the Level 1 trigger and furthermore to 400 Hz in the High-level trigger. This chapter is mostly based on [23], [18], [11] and [49].

5.1 Level 1 trigger

The CMS Level 1 trigger is a system which has to make its decisions in under 4 μs. To achieve this speed, it is completely hardware-based. As can be seen from the Schematic 5.1, it is divided into the calorimeter trigger and the muon trigger which are combined in the end in the Global Trigger. The muon trigger uses CSC, DT and RPC data.

5.1.1 Calorimeter trigger

The calorimeter trigger uses data from the ECAL, the HCAL and the HF, the Hadron Forward Calorimeters which are located at the ends providing coverage for large pseudorapidities. The signal data is geometrically combined into *trigger towers*. The first trigger layer consists of 18 processor boards which receive trigger towers from specific geometrical regions. They take care of the trigger tower level preprocessing such as calibrating the tower energies. The second layer consists of nine processor boards. The whole event is given to a single processor which can evaluate it in its entirety. This layer calculates the global energy variables such as the missing transverse energy.

5.1.2 Muon trigger

In the current trigger system the data from all three parts of the muon chambers are used to reconstruct the muon tracks. The Muon track finder layer is divided

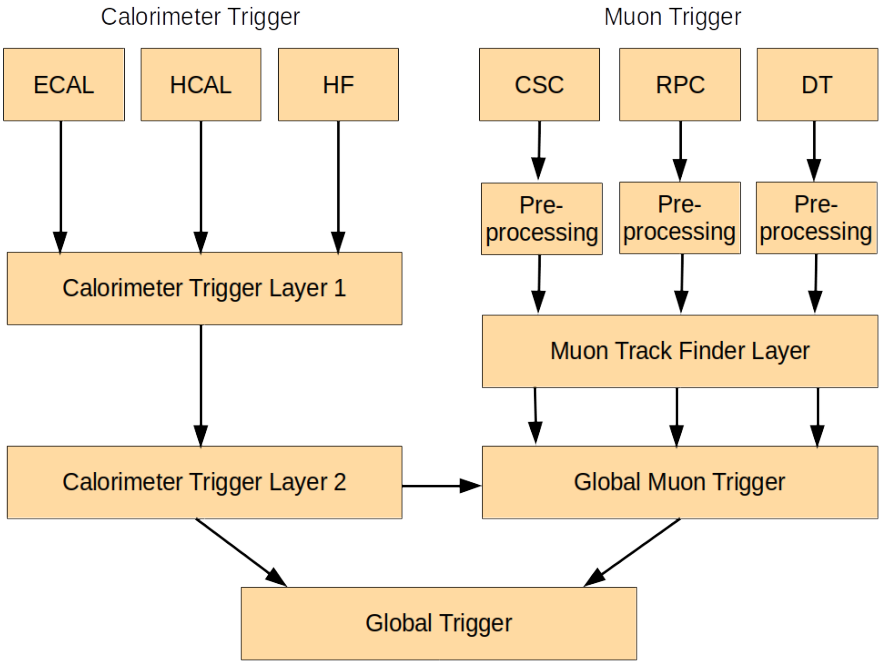

Figure 5.1: The structure of the CMS Level 1 trigger system in Run 2.

into three parts, the endcaps, the muon barrels and the overlap region. Their outputs are combined in the Global Muon Trigger which ranks the muon candidates by transverse momentum and quality. Also input from the Calorimeter Trigger is available to calculate the isolation of the muons.

5.1.3 Global trigger

The Global Trigger combines the data acquired from the calorimeter and muon triggers. Firstly, the input data from the calorimeter and the muon triggers must be synchronized to the LHC clock and to each other. The global trigger contains the list of active triggers and uses it to make the decision on whether to accept or discard an event. It takes into account the transverse energy, momentum and quality of the event and combines these using logical operators (NOT, OR, AND). The conditions may be used either as triggers or as veto conditions.

In addition the event must satisfy the so-called *trigger rules*. Those are designed to prevent buffer overflows in the data acquisition system by for example requiring enough time between two accepted bunch crossings. The global trigger has been upgraded during early Run 2 to allow more complex trigger paths that used to be implemented in the high level trigger. This allows more specialized L1 triggers calculating for example invariant masses [52].

5.2 High level trigger

The CMS high level trigger (HLT) is a fully software-based triggering system [4]. It runs on the *event filter farm* located close to the CMS detector. The farm consists of commercial computers running Scientific Linux and has approximately 30,000 CPU cores.

The output is limited by the bandwidth of the data transfer to the CMS Tier 0 data storage. Therefore the HLT must reduce the data taking frequency to under 1 kHz. The HLT contains hundreds of so-called *HLT paths* which are sets of algorithmic steps run in the order of increasing complexity and making the selection of accepted events.

The HLT is the first instance where the tracking data is taken into account. To make use of it, the HLT runs a simplified version of the Particle Flow algorithm which is an event reconstruction program used in the offline analysis. One more advantage of using tracking data is that it can distinguish electrons from photons since electrons, unlike photons, leave a track in the detector.

During Run 2 the HLT contained approximately 400 different trigger paths. Most of them make heavy use of HLT-level particle reconstructions, muons, electrons, photons and hadrons. These PF candidates can also be used to construct higher level objects such as tau or b jet candidates.

The HLT works in two distinct steps and can therefore be divided into the Level 2 and Level 3 triggers. The first step, the Level 2 trigger typically only uses information from the muon detectors and the calorimeter. The Level 3 then includes the full track reconstruction in the tracker. A mix between the Level 2 and the Level 3 triggers is called the Level 2.5 trigger and it uses partial tracker information, for example hits in the pixel detector. The Level 2 track reconstruction for charged particles is based on the combinatorial Kalman filtering [47].

The HLT is seeded by isolated seeds from the the Level 1 trigger. The criterion for isolation was tightened in 2016 to keep the trigger rate under control with the increased luminosity at the LHC [21].

The HLT performance is monitored by online and offline Data Quality Monitoring (DQM). The object efficiency for the CMS data is measured using the *Tag and Probe* method [20]. In it the object resonances are constructed both with a tight identification (tag) and a more relaxed identification (probe). The shapes for (tag + probe passed) and (tag + probe failed) are fitted separately to the signal+background and the efficiency is computed from the signal yield ratio between the two shapes.

5.3 Tau and MET triggers

In this thesis we are interested in triggers identifying events containing tau leptons and/or MET. For the $H^+ \to \tau\nu$ decay the decay products are a tau lepton, neutrino, two b jets and two light quark jets. However, the b jets are very soft and therefore often we might not be able to reconstruct them. Since the tau lepton and the

neutrino are the most energetic objects out of the decay products, these are used in the triggering.

The three triggers used in this thesis were:

1. HLT_200MET (referred to as the singleMET trigger)
2. HLT_VLooseIsoPFTau120_Trk50_eta2p1 (referred to as the singleTau trigger)
3. HLT_LooseIsoPFTau50_Trk30_eta2p1_MET90 (referred to as the tau+MET trigger)

For singleMET trigger the Level 1 seed was `L1_ETM50 OR L1_ETM60 OR L1_ETM70 OR L1_ETM80 OR L1_ETM90 OR L1_ETM100 OR L1_ETM120`. If one of the L1 seeds is disabled, a back up seed takes its place and therefore the OR clause is so long. In 2016 the lowest unprescaled L1_ETM seed was `L1_ETM80`. For the MET triggers two algorithms can be used to calculate the missing transverse energy, CaloMET and PFMET. The CaloMET algorithm sums over all energies in the calorimeter trigger towers. This is used in our analysis. The reason of using CaloMET instead of PFMET is that embedding is an option to be used in this analysis, even though it was not used in this work. In embedding the MET energy must be recalculated and the offline and trigger CaloMET values are closer to each other than the corresponding PFMET values. For the singleMET trigger the transverse momentum threshold was 200 GeV.

For singleTau trigger the Level 1 seed was `L1_SingleTau80er OR L1_SingleTau100er`. For the tau triggers the hadronic tau leptons must be separated from the quark and gluon jets. This is done by requiring that the tau leptons are *isolated*. For the tau leptons the isolation working point is very loose. It is required that there are only small energy deposits in seven out of eight non-central trigger regions. The jet energy deposit must also be contained in a 2x2 square of trigger towers [23]. Also there is a cut for the leading track transverse momentum. It is required to be over 30 GeV.

The events are also classified according to the number of *prongs* in the event. The number of prongs tells the number of charged hadrons in the decay mode. The trigger chooses events with 1-3 prongs in the hadronic decay. The analysis then targets the decays with 1 prong. For the singleTau trigger the transverse momentum threshold was 120 GeV. The Level 2 trigger for singleTau uses CaloTau (hltSingleL2Tau80eta2p2) and the backup trigger is HLT_VLooseIsoPFTau140_Trk50_eta2p1.

The search for charged Higgs bosons in the fully hadronic $\tau\nu$ final state currently selects interesting events with a tau+MET trigger. For the tau+MET trigger the efficiencies of the tau and MET parts are assumed to be uncorrelated and they are also calculated separately for the data and the simulations. In July 2016 the tau+MET80 trigger was disabled and the analysis moved to using tau+MET90 trigger as a back up. The Level 1 seed for tau+MET90 was `L1_ETM80 OR L1_ETM90 OR L1_ETM100`. This tau+MET trigger is designed to require a tau lepton with a

threshold energy of 50 GeV and a pseudorapidity $|\eta| < 2.1$ as well as a neutrino (MET) with a threshold energy of 90 GeV. The τ candidate is also required to be loosely isolated and the leading track from the tau lepton must have a transverse momentum of at least 30 GeV.

The Level 2 trigger for tau+MET is CaloMET (module: hltMET90) and MET cleaning (module: hltMetClean) is applied to it. The Level 2.5 pixel isolation is used as well as the Level 3 trigger system. Tau+MET Level 2.5 trigger uses tracks that have only been reconstructed using the pixel detector. The reason is that this drops the event rate going into PF reconstruction, so that this stage does not slow the trigger system down too much. The Level 3 trigger uses a simplified PF which requires less hits to the detector than offline PF.

6. Charged Higgs boson analysis in the fully hadronic final state

In this analysis we must simulate not only the physics processes but also the detector response to both the background and the target particle, the charged Higgs boson. The goal is to select as high concentration of signal events as possible while accurately estimating the irreducible background. If we would detect an excess of charged Higgs boson decay products, in this case τ and ν, it could be a sign of the existence of the said particle. In this analysis we are only interested in tau leptons that decay into hadrons. The hadronically decaying tau lepton is denoted as τ_h. More information about the analysis can be found on [46].

6.1 Invariant mass

A useful quantity in particle physics is the invariant *transverse mass*. It is defined as

$$m_T^2 = m^2 + p_x^2 + p_y^2 = E^2 - p_z^2 \tag{6.1}$$

It is invariant with respect to Lorentz boosts along the z direction. A related quantity is the transverse energy E_T defined as:

$$\bar{E_T} = E\frac{\bar{p_T}}{|\bar{p}|} = \frac{E}{\sqrt{E^2 - m^2}}\bar{p_T} \tag{6.2}$$

where the transverse momentum vector $\bar{p}_T$ is (p_x, p_y). At the high-energy limit $(m = 0)$ all three transverse quantities are the same: $m_T = E_T = p_T$.

The charged Higgs boson transverse mass depends on the transverse energies of the tau jet (E_T^τ) and the neutrino (E_T^M) as well as the angle between them $(\Delta\phi(\tau_h, \bar{p}_T^M))$ as seen in Formula 6.3 below. Therefore these must be measured very accurately and the uncertainties in these measurements must be accurately assessed.

$$m_T = \sqrt{2E_T^\tau E_T^M(1 - \cos(\Delta\phi(\tau_h, \bar{p}_T^M)))} \tag{6.3}$$

6.2 Offline event selection

In the *event selection* the goal is to reduce the background while retaining as much of the signal as possible. The first event selection is already done at the trigger level,

which is often referred to as the *online selection*. This was described in previous sections. It is contrasted by the *offline selection* which is done afterwards for the events that passed the online selection. The selection criteria are briefly described below.

Since a major part in the final results is played by the neutrino energy, it is important to make sure that the MET values are correct and filter out those that contain anomalous MET, likely caused by mistakes or measurement uncertainties in particle reconstruction as well as detector malfunctions. This is done using *data quality filters*. These are described in detail in [26].

In the analysis a robust cut based signal selection is chosen. The primary vertex needs to be the one with the largest p_T. We select one-prong τ_h candidates, corresponding to decays into a charged pion and up to two neutral pions. The events are required to have at least three jets with $p_T > 30$ GeV and $|\eta| < 4.7$.

In the fully hadronic final state there should be no electrons or muons present. Therefore we reject the events with isolated electrons with $p_T > 15$ GeV and $|\eta| < 2.5$ as well as muons with $p_T > 10$ GeV and $|\eta| < 2.5$.

We require at least one of the jets to be identified as a b jet with $|\eta| < 2.4$. This criterion leaves most of the genuine b jets while reducing the amount of misidentified b jets by two orders of magnitude.

We also make some angular selections. At this point the background is dominated by QCD multijet events where a jet is misidentified as τ_h and its momentum is incorrectly estimated, creating MET. This background is suppressed by requiring the angles between the jets and the missing transverse energy to satisfy the following:

$$R_{\mathrm{bb}}^{\mathrm{min}} = \mathrm{min}_n\Big(\sqrt{(180^\circ - \Delta\phi(\tau_h, \bar{p}_T^M))^2 + (\Delta\phi(\mathrm{jet}_n, \bar{p}_T^M))^2}\Big) > 40^\circ \qquad (6.4)$$

The index n runs over the jets with the three highest p_T values.

The data can be categorized using the variable $R_\tau = p_{\text{leading track}}/p_\tau$. In that case the small and large values for this variable are analyzed separately and combined statistically at the end of the analysis.

6.3 Background estimation

Understanding the relevant background processes is very important. For the $\tau_h\nu$ analysis the dominant background processes are the $t\bar{t}$ production and the QCD multijet background. Other backgrounds that are present are the single top quark production, the diboson production, the W boson production in association with jets and the Z/γ^* processes. We can classify the backgrounds into genuine-tau events and misidentified fake taus. From Image 6.1 we can see that the fake tau background is more prominent with higher tau lepton transverse masses.

The genuine-tau background is estimated using simulations. We trust the genuine-tau simulations since *embedding* and simulations match well. Embedding is a technique to estimate genuine tau Standard Model backgrounds based on data [25]. It uses reconstructed μ events and replaces the muons with taus with the same

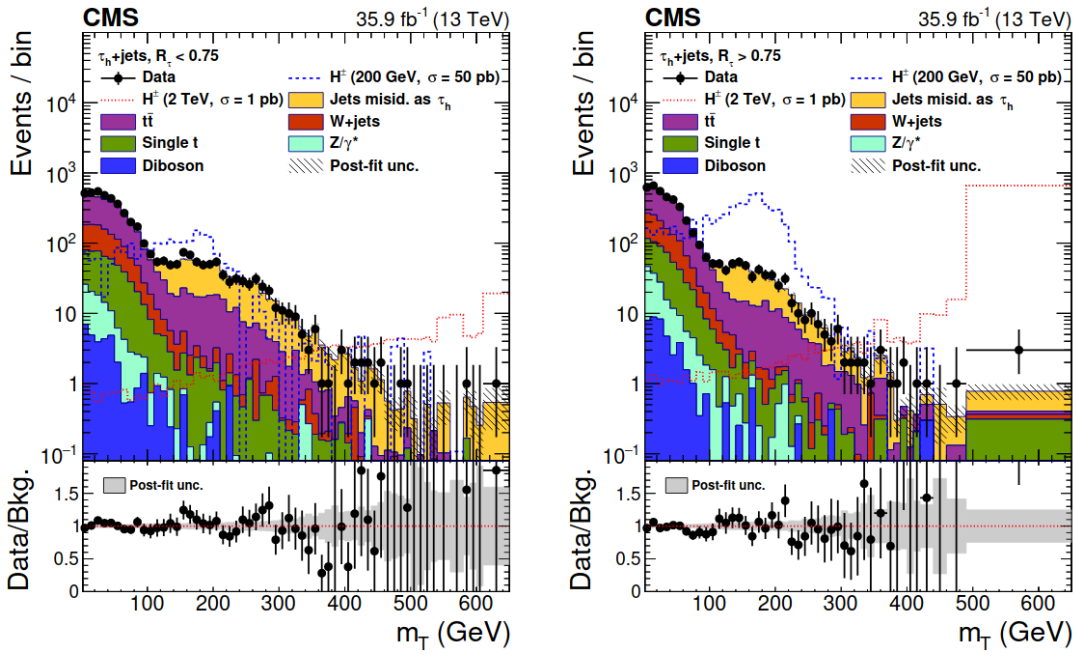

Figure 6.1: The τ_h+jet final state transverse mass distributions with a background-only fit to the data. The data is divided based on the variable $R_\tau = p_{\text{leading track}}/p_\tau$ so that the events with $R_\tau < 0.75$ is plotted on the left and $R_\tau > 0.75$ on the right. [46]

kinematic properties. Embedding has been studied for this process but it is not currently part of the $H^\pm \to \tau\nu$ analysis.

The fake tau background is estimated using a *control region* which has no signal and comparing it to the background in the signal region. The control region uses an *altered selection*. It only accepts very loosely isolated τ_h candidates which do not pass the normal selection. From this we can derive *transfer factors* that are used to normalize the background. The jets from the QCD multijet events and the top/electroweak events have different quark and gluon compositions so their transfer factors are estimated separately and a weighted average is used.

6.4 Systematic uncertainties

The limited precision of a measurement is estimated by determining the uncertainties. These uncertainties consist of statistical and systematic uncertainties. For this analysis one of the most relevant sources of systematic uncertainties is related to the efficiency of the triggers.

If the trigger was exactly accurate, the trigger efficiency turn-on curve would be a step function. However, inaccuracies in measurements smear the curve. Also, the simulation and the data don't match exactly, as seen in Fig 6.3. They need to be fitted using *scale factors*.

We can define *trigger efficiency* ϵ, which is calculated for the data and the

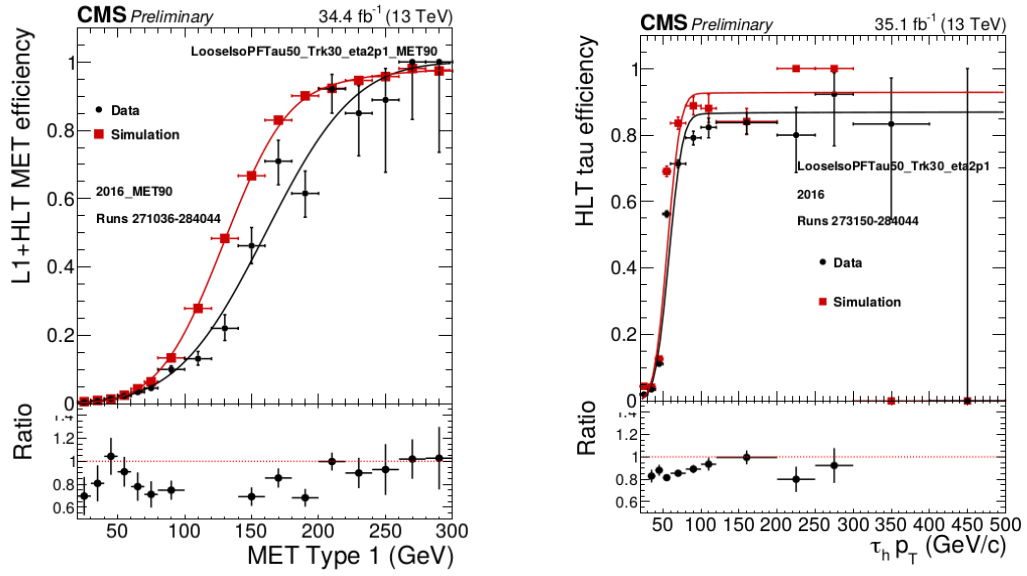

Figure 6.2: The trigger turn on plots for the MET leg and the Tau leg in Tau+MET trigger.

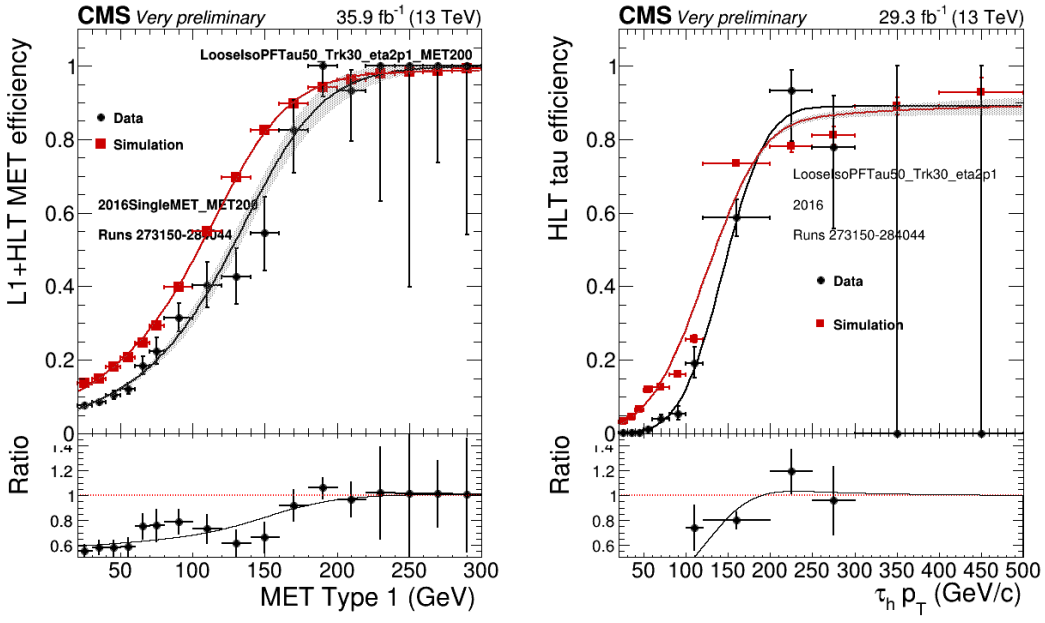

Figure 6.3: The trigger turn on plots for the MET leg in the singleMET trigger and the Tau leg in the singleTau trigger.

simulation separately. The simulations are matched to the data using the scale factors:

$$\mathrm{SF} = \frac{\epsilon_{\mathrm{data}}}{\epsilon_{\mathrm{sim}}} \tag{6.5}$$

The uncertainties for the scale factors can be found by varying both trigger efficiencies independently.

$$\begin{aligned} \mathrm{SF}_{\mathrm{data,up}} &= \frac{\epsilon_{\mathrm{data}} + \sigma^{\mathrm{up}}_{\mathrm{data}}}{\epsilon_{\mathrm{sim}}} \\ \mathrm{SF}_{\mathrm{data,down}} &= \frac{\epsilon_{\mathrm{data}} - \sigma^{\mathrm{down}}_{\mathrm{data}}}{\epsilon_{\mathrm{sim}}} \\ \mathrm{SF}_{\mathrm{sim,up}} &= \frac{\epsilon_{\mathrm{data}}}{\epsilon_{\mathrm{sim}} + \sigma^{\mathrm{up}}_{\mathrm{sim}}} \\ \mathrm{SF}_{\mathrm{sim,up}} &= \frac{\epsilon_{\mathrm{data}}}{\epsilon_{\mathrm{sim}} - \sigma^{\mathrm{down}}_{\mathrm{sim}}} \end{aligned} \tag{6.6}$$

The other sources of uncertainties include for example tau identification and isolation, lepton identification and isolation, b jet identification, lepton scale and resolution, pileup uncertainties and luminosity uncertainties. For the tau leptons with the highest transverse momenta some extra uncertainties are applied. For the backgrounds taken from simulations, the cross section is varied within the theoretical uncertainty. An example of the effects of the uncertainties can be seen on Table 6.1.

The systematic uncertainties can be divided in two categories. They may either only modify the event yields or also the shape of the final transverse mass distributions. In the latter case they are called *shape uncertainties*. Whether an uncertainty is a shape uncertainty or not is indicated in the table as well.

Source	Shape	$H^{\pm}$ (200 GeV)	Jets $\rightarrow \tau_h$	$t\bar{t}$	Single t	Electroweak
τ+MET trigger efficiency	yes	10.3	2.0	9.0	7.3	7.4
τ_h identification	yes	4.2	0.6	4.0	4.0	4.1
Lepton veto efficiency	no	0.3	-	0.4	0.3	<0.1
Jet energy scale and resolution	yes	4.8	0.4	2.0	2.2	4.3
τ_h energy scale	yes	1.8	0.6	2.2	2.1	2.3
Unclustered MET energy scale	yes	0.6	<0.1	<0.1	<0.1	< 0.1
b jet identification	yes	3.5	0.8	2.9	2.9	2.5
Integrated luminosity	no	2.5	0.4	2.5	2.5	2.5
Pileup	yes	0.6	<0.1	<0.1	<0.1	<0.1
Jets misid. as τ_h estimation	yes	-	6.1	-	-	-
Cross section (scales, PDF)	no	-	0.8	5.5	5.3	3.3
Top quark mass	no	-	0.4	2.8	2.2	-
Acceptance (scales, PDF)	no	5.1	0.5	2.8	2.8	6.8
Total		14.0	6.6	12.9	11.6	13.9

Table 6.1: The effect of systematic uncertainties on the final event yields (in per cent) before the fit and summed over the R_τ categories. The mass point 200 GeV is chosen for the charged Higgs boson as an example. [37]

7. Results

In *categorization* we divide the data into multiple parts according to some criteria. The statistical analysis is then applied to the parts separately and only combined at the very end. This is found to improve the sensitivity of the analysis in some cases. The $H^{\pm} \to \tau\nu$ analysis described in [46] used categorization based on the variable R_τ. In this thesis the R_τ categorization was not used, the following categorizations were compared to a non-categorized case.

7.1 Categorization by passed trigger

Although the tau+MET trigger is used in the reference analysis, it is not the only possibility for selecting events for the analysis. The ATLAS collaboration uses a singleMET trigger in their analysis of $H^{\pm} \to \tau\nu$. The threshold they use is 70, 90 or 110 GeV depending on the data-taking period. The problem with it is that it is harder to probe the entire $H^{\pm}$ mass regime using the data that passes this trigger [5].

In this work we use data from three triggers. The most important aspect is that they accept events with different energy thresholds:

1. **singleMET trigger** which requires the event to have a MET with $p_T > 200$ GeV
2. **singleTau trigger** which requires the event to have a tau lepton with $p_T > 120$ GeV
3. **tau+MET trigger** which requires the event to have a tau lepton with $p_T > 50$ GeV and MET with $p_T > 90$ GeV.

A more thorough explanation of the triggers was given in Section 5.3. The last one of the listed triggers is the trigger which is currently used in the analysis. There were possible advantages in using single triggers instead of the tau+MET trigger. Taking data passing a singleMET trigger means that we can get rid of some uncertainties relating to the trigger itself. By using a single trigger, we do not have the uncertainty of the other object contributing to the systematic uncertainty.

Additionally in that case we do not need to assume that the uncertainties of the tau and MET legs are uncorrelated. In reality the uncertainties have some correlation. Based on this we decided to build a *trigger categorization system*, which uses single object (singleMET and singleTau) triggers whenever they have fired, and the tau+MET trigger only when neither of the single object triggers fired.

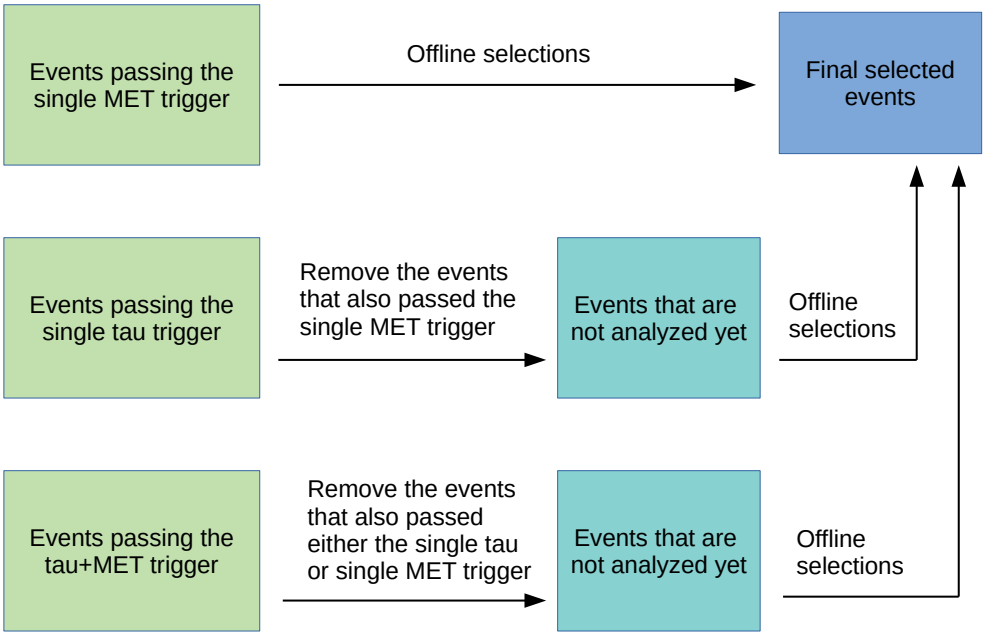

Figure 7.1: The structure of the full trigger combination.

One event may pass multiple triggers. In this case the event is taken through the trigger that is listed first in the list above. This process is described in Figure 7.1. In order to compare the effects of the single triggers separately, we also ran versions that combine data only from one of the single triggers with the tau+MET trigger. The structure of those can be seen in Figure 7.2.

The possible improvement in the analysis accuracy was assessed by determining limits on the production rate in the studied channel. The limits show the minimum value for the quantity $\sigma_{H^{\pm}} \times B_{H^{\pm} \to \tau\nu}$ with the condition that it must still be detected by the analysis. The main goal was to reduce the systematic uncertainties, which is shown as the confidence intervals getting narrower. The study brought up an unexpected change in the limit median, and this effect was being investigated as a secondary effect.

For the trigger categorization we compared the trigger combinations to the original tau+MET trigger case. The median values as well as the $\pm 1\sigma$ confidence intervals are tabulated in the Tables 7.1, 7.2 and 7.3 respectively. The widths of the $\pm 1\sigma$ confidence intervals are plotted in Figure 7.3. The combination of the tau+MET and singleTau triggers is found to narrow the confidence intervals in the high $H^{\pm}$ mass range.

In Figures 7.4 and 7.5 we can see the median expected limit lines of the different trigger categorizations and the original tau+MET trigger case. We see that the limit medians are much lower in the trigger combinations. Combining the tau+MET

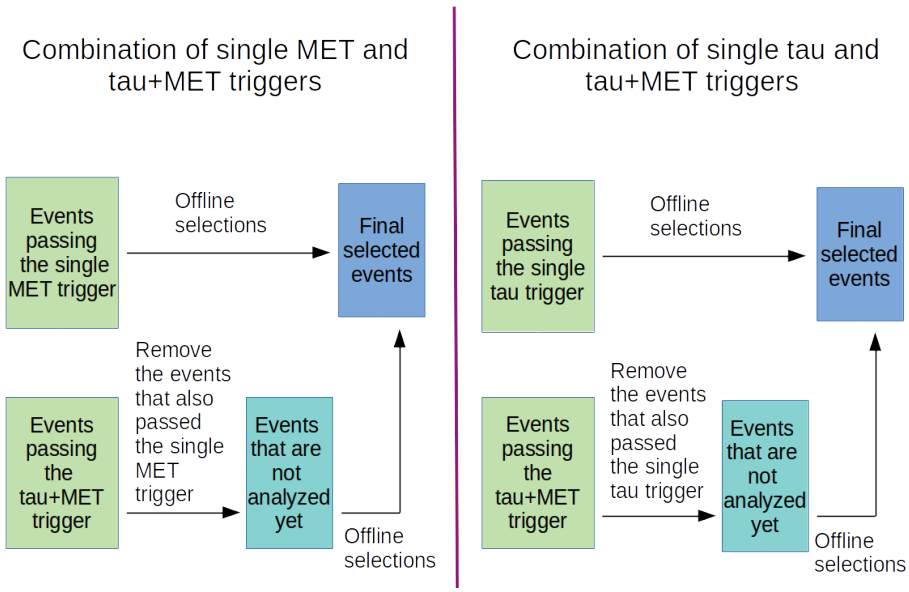

Figure 7.2: The structure of the partial triggers used to assess the effect of the singleMET and singleTau triggers separately.

and the singleMET triggers results in limit medians approximately 0.6 times the tau+MET trigger case for large $H^{\pm}$ values. For the combination of the tau+MET and singleTau triggers the same result is approximately 0.4 times the control case. For the full categorization of triggers the line is slightly lower than that and it provides the very highest effect in this regard. It also seems that most of the contribution for the effect comes from the MET categorization.

Looking at Figure 7.6 we can see that in the lowest surveyed $H^{\pm}$ masses the majority of events go through the original tau+MET trigger. For large charged Higgs boson masses the majority of the events pass the singleMET trigger. This makes sense, since the decay products of a heavier boson are more likely to have higher momenta, letting the MET to pass the turn-on transverse momentum of the singleMET trigger. Since the singleMET trigger was the primary choice of a trigger for an event to come through (see Fig 7.1) the events that pass both singleMET and singleTau triggers are taken through the singleMET trigger. Conversely, if the singleTau trigger is taken as the primary choice, as in Fig 7.7, most events go through the singleTau trigger for the heavy charged Higgs bosons.

Trigger categorization: medians

m(H^+)	Tau+MET	full categorization	singleTau and tau+MET	singleMET and tau+MET
180	1.44062	0.75313	0.88125	0.93750
200	0.89375	0.52188	0.57500	0.65000
220	0.60469	0.42344	0.43437	0.49062
250	0.39219	0.27734	0.28906	0.30156
300	0.19141	0.16016	0.14648	0.16484
400	0.06777	0.03213	0.04648	0.03457
500	0.03203	0.01162	0.01943	0.01309
800	0.00693	0.00283	0.00400	0.00303
1500	0.00459	0.00205	0.00264	0.00225
2000	0.00459	0.00205	0.00264	0.00225

Table 7.1: The limit medians for the different trigger combinations and the tau+MET trigger as a reference. All results are obtained using data from 2016.

Trigger categorization: $+1\sigma$/median

m(H^+)	Tau+MET	full categorization	singleTau and tau+MET	singleMET and tau+MET
180	1.40658	1.50622	1.48156	1.46809
200	1.40260	1.49027	1.48036	1.46154
220	1.40259	1.47034	1.44419	1.43673
250	1.41054	1.47833	1.42414	1.45667
300	1.42647	1.47827	1.40667	1.48750
400	1.48237	1.74136	1.52174	1.65714
500	1.53013	1.77367	1.57895	1.73846
800	1.64646	1.73498	1.62250	1.66667
1500	1.68627	1.73171	1.60227	1.66667
2000	1.71678	1.73171	1.60227	1.66667

Table 7.2: The limit $+1\sigma$ confidence values relative to the median for the different trigger combinations and the tau+MET trigger reference case.

Trigger categorization: -1σ/median

m(H^+)	Tau+MET	full categorization	singleTau and tau+MET	singleMET and tau+MET
180	0.72150	0.67773	0.69674	0.68298
200	0.72388	0.68261	0.72143	0.69385
220	0.72149	0.69238	0.71860	0.70204
250	0.71552	0.68263	0.70690	0.69667
300	0.71433	0.68656	0.68667	0.72500
400	0.68998	0.56427	0.65217	0.57143
500	0.67125	0.55422	0.68421	0.57846
800	0.61183	0.57244	0.62000	0.61667
1500	0.61002	0.59024	0.59091	0.59556
2000	0.61002	0.59024	0.59091	0.59556

Table 7.3: The limit -1σ confidence values relative to the median for the different trigger combinations and the tau+MET trigger reference case.

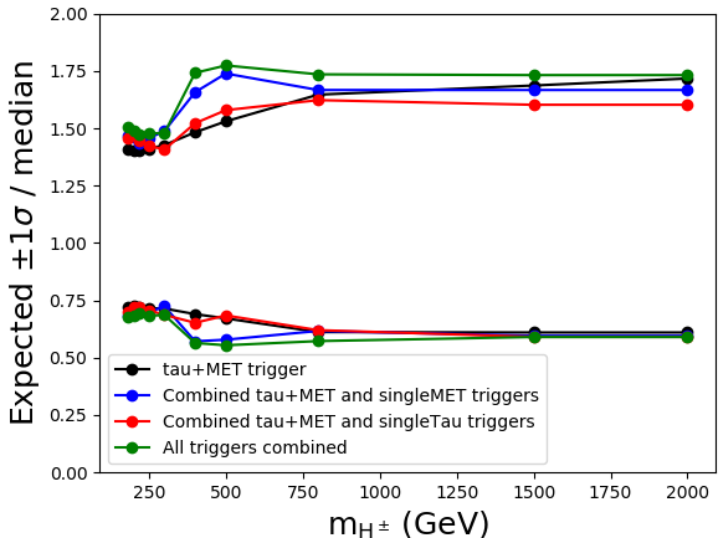

Figure 7.3: The widths of the 1σ confidence limits relative to the median for the tau+MET method and the trigger combinations.

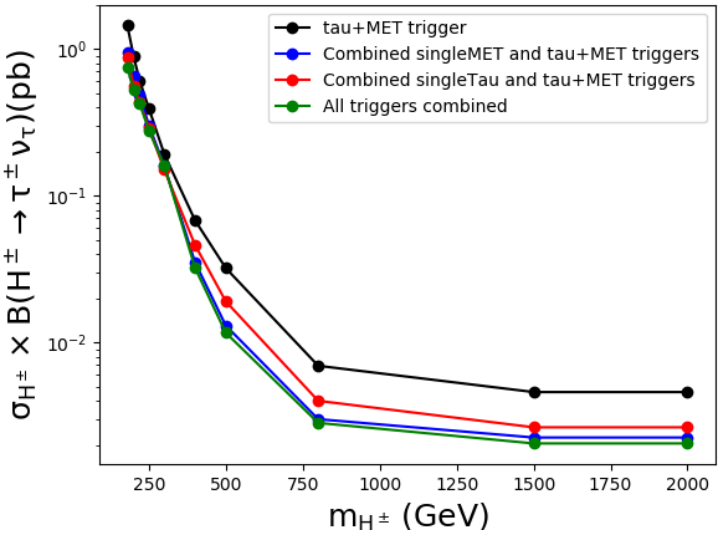

Figure 7.4: The median limit lines of the tau+MET trigger method as well as all three trigger combinations.

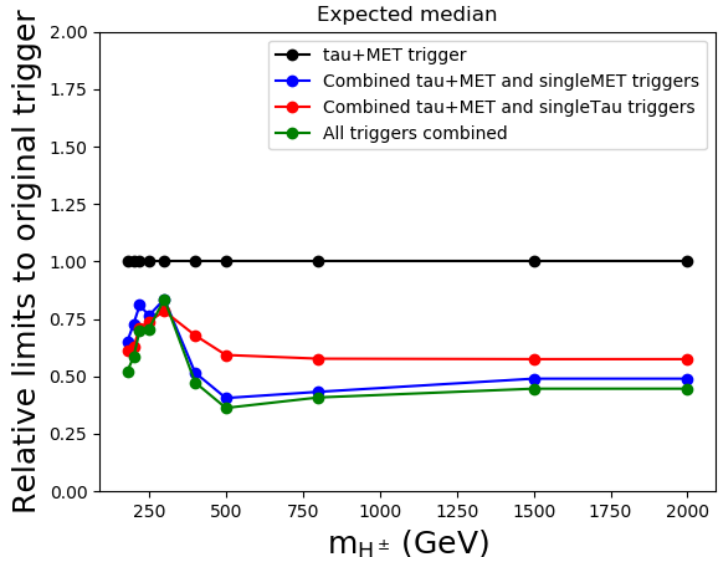

Figure 7.5: The median limit lines of the three trigger combinations compared to the tau+MET trigger.

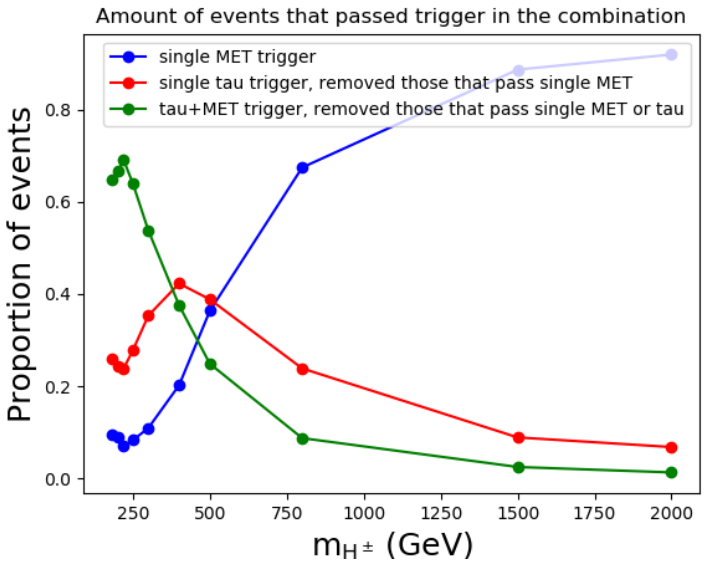

Figure 7.6: The number of events passing each trigger in the full trigger combination.

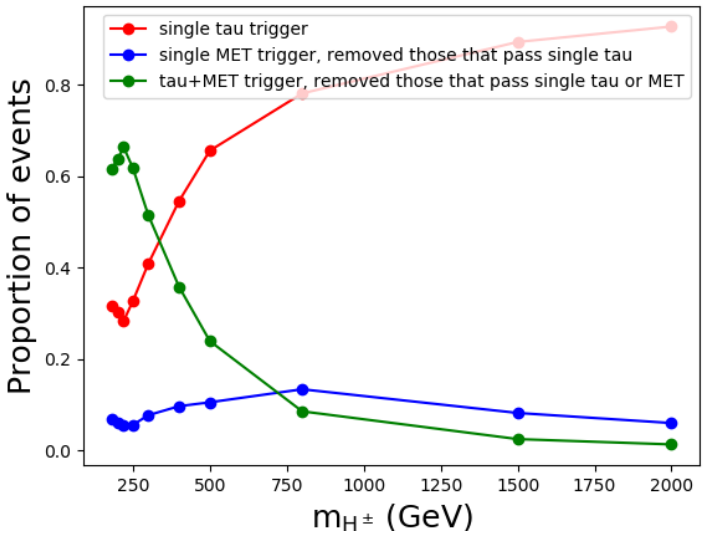

Figure 7.7: The number of events passing through each trigger when the singleTau trigger is taken as the first trigger to pass the events through.

7.2 Categorization by offline transverse momentum

The method described in the previous section divides the events based on their transverse momentum at the trigger level. In order to understand if the detected effects are based on the transverse momentum categorization we also tested cate-

gorization based on the transverse momenta in the offline stage. This can be used to try to explain the results of the trigger categorization. The offline categorization can be done using the transverse momenta of either the tau lepton or the MET. Both approaches as well as their combination were tested. The trigger used was the tau+MET trigger. Same leading track cuts were used as in the trigger categorization.

In order to be able to easily compare the results with trigger-based categorization, the cutoff points for the offline transverse momentum were chosen to have the same values as the trigger transverse momentum cuts.

For the tau lepton transverse momentum categorization the data was divided into the low transverse momentum sector with 50 GeV $< p_T^\tau <$ 120 GeV and the high transverse momentum sector with $p_T^\tau >$ 120 GeV.

For the MET event transverse momentum categorization the data was divided according to Particle Flow p_T^{miss} into the low transverse momentum sector with 90 GeV $< p_T^{\text{miss}} <$ 200 GeV and the high transverse momentum sector with $p_T^{\text{miss}} >$ 200 GeV. The Particle Flow variable is a more accurate variable than the CaloMET used in the trigger. An effect on the limits due to the MET measurement should be visible in both PFMET and CaloMET. However, offline CaloMET could also be used here since it would be a more exact comparison with the trigger categorization. The structure of these offline transverse momentum categorization schemes is pictured in Figure 7.8.

To emulate the trigger categorization, the events were divided in a specific way. The way to divide the events to accomplish this is best visualised as a square, as in Figure 7.9. The categories are chosen so that the offline categories correspond to the full trigger categorization.

The exact results for each combination can be seen on Tables 7.4, 7.5 and 7.6. The confidence intervals (Figure 7.10) stay generally similar compared to the control case, getting slightly wider mainly in the 400 GeV range. The offline tau transverse momentum categorization has a narrower interval than the MET or the full categorization. From Figures 7.13 and 7.14 we see that in both of the offline pT categorizations the high transverse momentum section catches more events in the higher $H^\pm$ masses.

For the limit median lines the offline categorization showed similar changes than the trigger categorization albeit in a smaller scale (Figures 7.11 and 7.12). The shapes of the limit lines compared to the control case are still similar to the trigger categorizations, but this time the lines are closer to the originals. The full offline categorization actually has higher limit medians than the control for lower masses and the lowest limit medians for the heavy charged Higgs bosons.

The differences between the two categorization methods are probably caused by the uncertainties associated with the single object triggers. Since the offline categorization uses only the tau+MET trigger, these uncertainties are not present in the offline categorization method. However, there are also similarities between the two categorization methods meaning that the categorization itself has an effect on the limits. This could be tested further by running the offline categorization with the errors from the trigger categorization. Using this method we could separate the

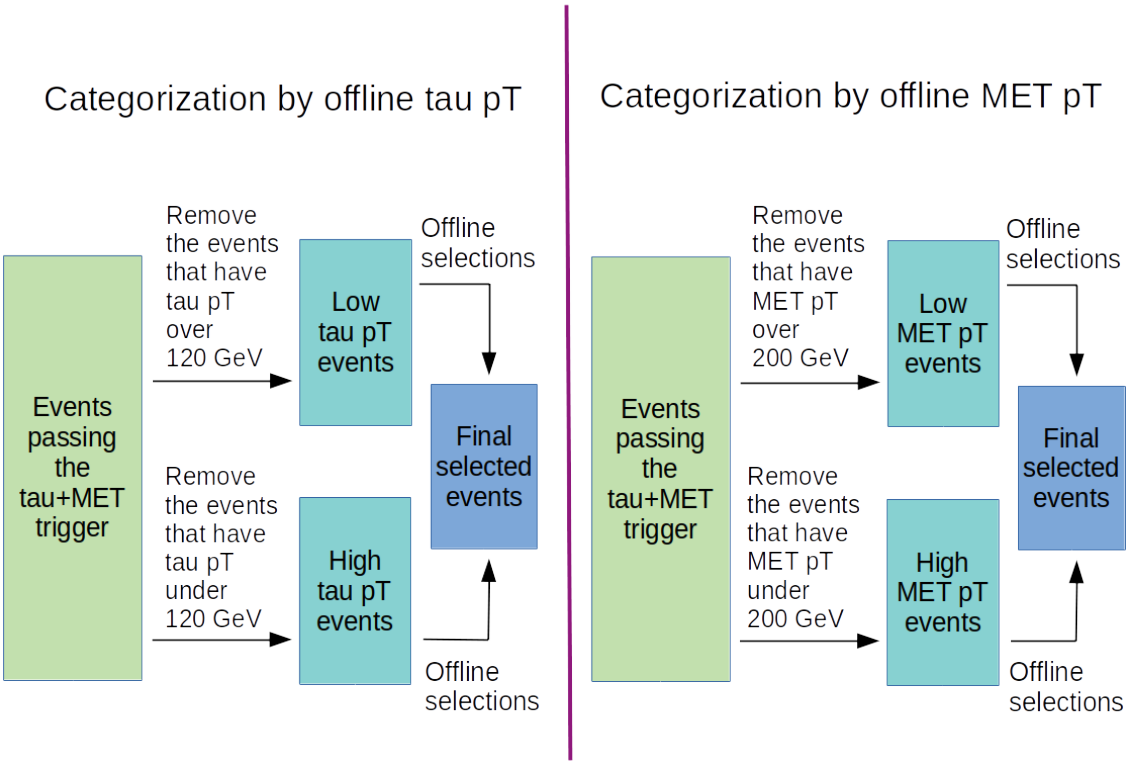

Figure 7.8: The structure of the offline categorization schemes for both the tau lepton and the MET offline transverse momenta.

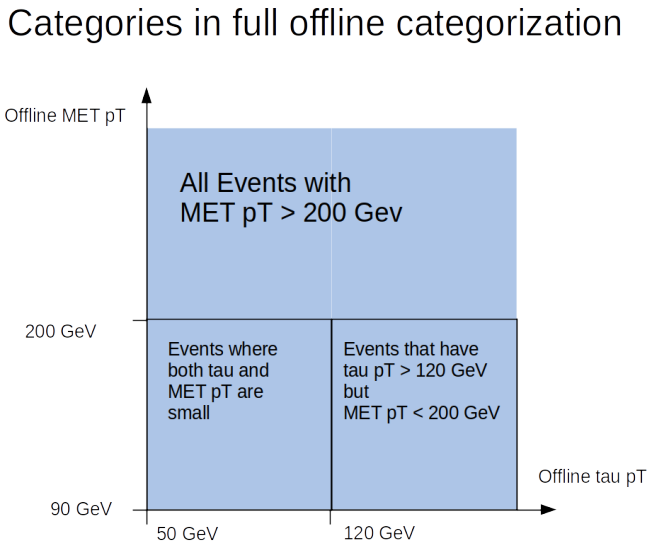

Figure 7.9: The different categories in the offline full categorization. These are combined at the end of the analysis in order to emulate the full trigger categorization.

effect caused by the single trigger uncertainties.

Offline pT categorization: medians

m(H^+)	Control	Offline tau pT categorization	Offline MET pT categorization	Full offline categorization
180	1.44375	1.13750	0.92813	1.12812
200	0.89688	0.72188	0.62813	0.97188
220	0.60625	0.57344	0.50156	0.83750
250	0.39219	0.36406	0.32031	0.48750
300	0.19297	0.18125	0.17969	0.23281
400	0.06797	0.05859	0.05000	0.05195
500	0.03213	0.02793	0.02207	0.02168
800	0.00693	0.00654	0.00586	0.00537
1500	0.00459	0.00439	0.00439	0.00381
2000	0.00459	0.00449	0.00439	0.00400

Table 7.4: The limit medians for the different offline transverse momentum categorizations and the case with no categorization as a reference. The control case is slightly different from the trigger categorization case due to technical reasons.

Offline pT categorization: $+1\sigma$/median

m(H^+)	Control	Offline tau pT categorization	Offline MET pT categorization	Full offline categorization
180	1.41032	1.43761	1.49014	1.53812
200	1.40201	1.44183	1.47440	1.50730
220	1.40317	1.41885	1.44936	1.48629
250	1.41921	1.43462	1.46737	1.49427
300	1.42228	1.45856	1.45242	1.49826
400	1.48162	1.55932	1.62000	1.66968
500	1.53551	1.59857	1.69231	1.70156
800	1.64646	1.66667	1.68601	1.68528
1500	1.70153	1.71982	1.71982	1.74803
2000	1.71678	1.71938	1.75171	1.70250

Table 7.5: The limit $+1\sigma$ confidence values relative to the median for the different offline transverse momentum categorizations and the case with no categorization as a reference.

Offline pT categorization: -1σ/median

m(H^+)	Control	Offline tau pT categorization	Offline MET pT categorization	Full offline categorization
180	0.72161	0.70562	0.68312	0.66382
200	0.72129	0.70083	0.69416	0.68554
220	0.72112	0.71379	0.70175	0.68506
250	0.71939	0.70604	0.69622	0.68176
300	0.70984	0.70166	0.70117	0.67694
400	0.69118	0.63729	0.61200	0.59711
500	0.67290	0.63441	0.59412	0.58948
800	0.62049	0.60703	0.60922	0.59962
1500	0.62092	0.62187	0.60137	0.60892
2000	0.62092	0.61024	0.62187	0.60000

Table 7.6: The limit -1σ confidence values relative to the median for the different offline transverse momentum categorizations and the case with no categorization as a reference.

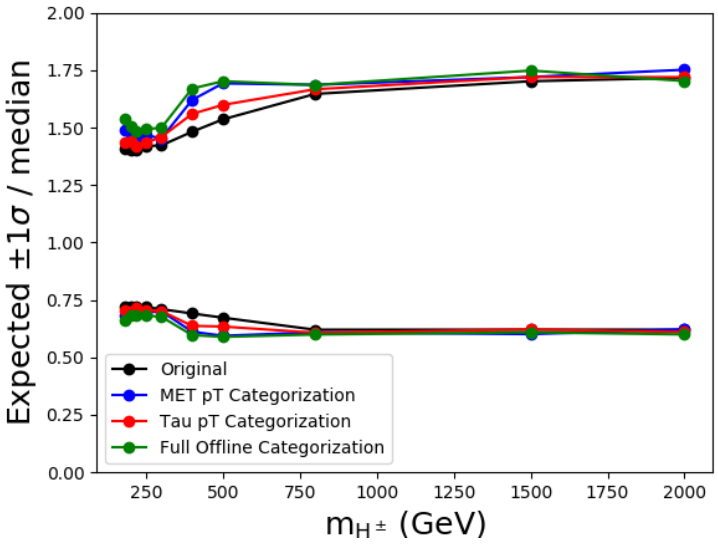

Figure 7.10: The widths of the 1σ confidence limits relative to the median for the control and the offline transverse momentum categorizations. MET pT categorization is according to PF MET.

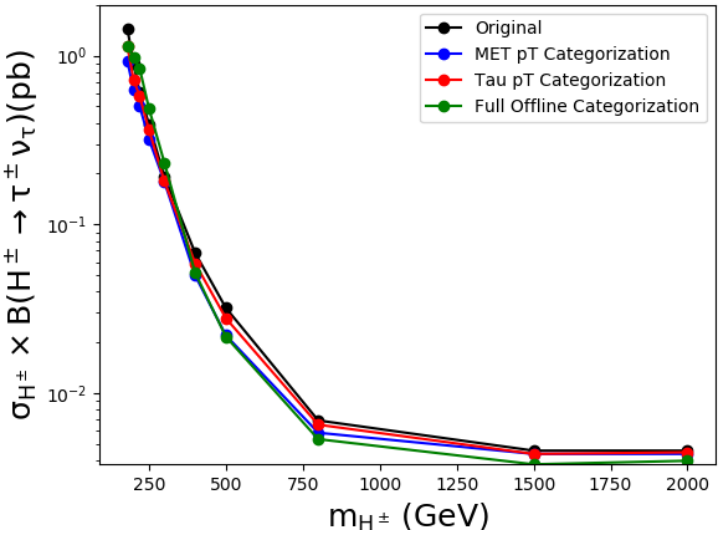

Figure 7.11: The median limit lines of the reference case and the offline transverse momentum categorizations.

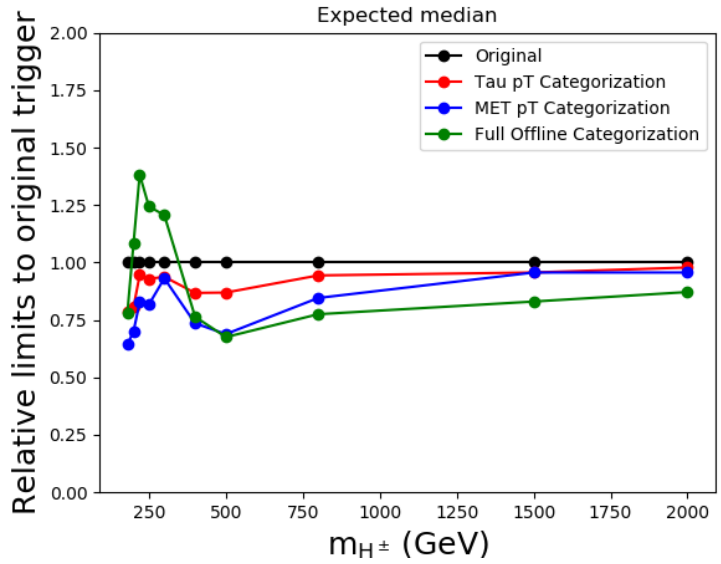

Figure 7.12: The median limit lines compared to the reference case.

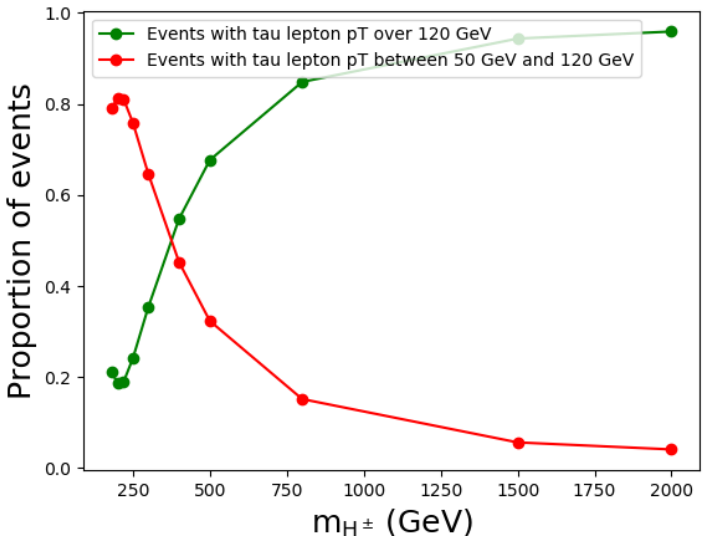

Figure 7.13: The number of events passing to different categories in offline tau lepton transverse momentum categorization.

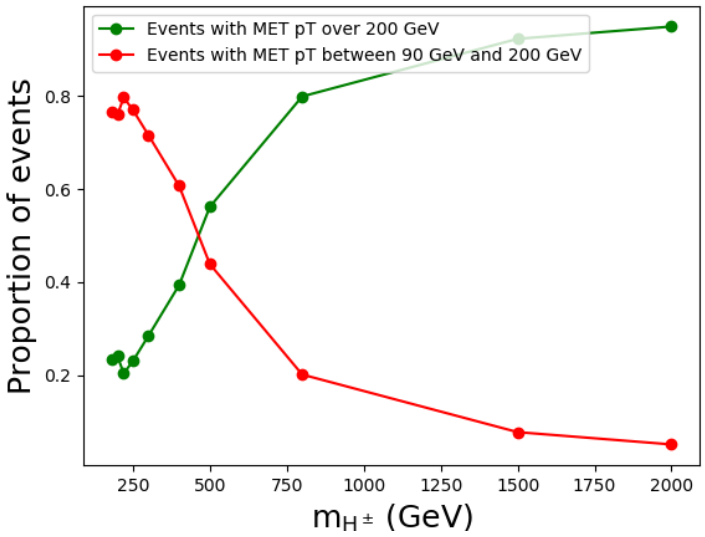

Figure 7.14: The number of events passing to different categories in offline MET transverse momentum categorization.

8. Conclusions

The goal of this thesis was to lower the trigger uncertainties in the $H^{\pm} \rightarrow \tau\nu$ analysis. Therefore we divided the samples based on which triggers were fired and then combined them statistically. The goal was to narrow the confidence intervals for the charged Higgs boson production limits. The widths of the $\pm 1\sigma$ confidence intervals can be seen in Figure 7.3. There is improvement in the TeV scale for some categorizations, but not in the lower mass range. Best results are obtained using the categorization with the singleTau trigger.

The effect on the limit median lines was unexpected. To shed light into this phenomenon, we emulated the trigger categorization by the corresponding offline objects. It turns out that in the case of the offline transverse momentum categorization the effect is smaller but still present.

The reason for the difference between the two categorization methods is probably due to the fact that the single triggers have their own uncertainties associated with them. These uncertainties are not present in the offline categorization scheme.

On the other hand, offline categorization still produces roughly similar results to the trigger case. They are also close to the ones obtained with the R_{τ} categorization schemes previously. There seems to be a limit median lowering effect present that is due to the categorization itself.

To find if the single trigger uncertainties affect the results, in the future we could try to compare the uncertainties of the different methods directly. The effects of the single trigger turn on and uncertainty could be studied in more detail. We could also run the offline categorization using the errors from the trigger categorization. In the future this categorization could also be tested along with the old R_{τ} categorization. Also, one could try to categorize all the triggers so that the singleTau trigger is the primary choice.

All in all, we have managed to improve the accuracy of the analysis in the TeV scale with some schemes such as the categorization using the singleTau and the tau+MET triggers. Interesting effects relating to the limit median lines were also found. This method of categorization is worth exploring further and it could well be used in the upcoming whole Run2 analysis. Further research in understanding the median line lowering effect and finding the optimal categorization scheme would also be interesting.

References

1 G. Aad et al. Observation of a new particle in the search for the Standard Model Higgs boson with the ATLAS detector at the LHC. *Physics Letters B*, 716:1–29, Sep 2012.

2 V. M. Abazov et al. Search for charged Higgs bosons in top quark decays. *Physics Letters B*, 682(3):278–286, Dec 2009.

3 G. Abbiendi et al. Search for Charged Higgs bosons: Combined Results Using LEP Data. *European Physical Journal C*, 73:2463, Jan 2013.

4 W. Adam et al. The CMS high level trigger. *European Physical Journal C*, 46:605–667, Nov 2005.

5 J. A. Aguilar Saavedra et al. Search for charged Higgs bosons decaying via $H^{\pm} \to \tau \pm \nu_{\tau}$ in the τ+jets and τ+lepton final states with 36 fb^{-1} of pp collision data recorded at $\sqrt{s} = 13$ TeV with the ATLAS experiment. *Journal of High Energy Physics*, 139, Sep 2018.

6 I. Aitchison. Supersymmetry and the MSSM: An elementary introduction. arXiv:hep-ph/0505105, Jun 2005.

7 G. Apollinari, O. Bruening, T. Nakamoto, and L. Rossi. *High Luminosity Large Hadron Collider HL-LHC*. Number CERN-2015-005 in CERN Yellow Reports: Monographs. May 2017.

8 D. Barney. CMS detector slice. https://cds.cern.ch/record/2120661. Accessed 19 June 2020.

9 G. Branco, P. Ferreira, L. Lavoura, M. Rebelo, M. Sher, and J. Silva. Theory and phenomenology of two-Higgs-doublet models. *Physics Reports*, 516, May 2011.

10 O. S. Brüning, P. Collier, P. Lebrun, S. Myers, R. Ostojic, J. Poole, and P. Proudlock. *LHC Design Report*. Number CERN-2004-003 in CERN Yellow Reports: Monographs. CERN, Geneva, Jul 2004.

11 L. Cadamuro. The CMS level-1 trigger system for LHC run II. *Journal of Instrumentation*, 12(03):C03021–C03021, Mar 2017.

12 M. Carena, S. Heinemeyer, O. Stål, C. E. M. Wagner, and G. Weiglein. MSSM Higgs boson searches at the LHC: benchmark scenarios after the discovery of a Higgs-like particle. *The European Physical Journal C*, 73(9), Sep 2013.

13 CERN. $H^{\pm}$ branching ratio plots. https://twiki.cern.ch/twiki/bin/view/LHCPhysics/LHCHXSWGCrossSectionsFigures#H_BR_plots_MSSM. Accessed 19 June 2020.

14 S. Chatrchyan et al. Observation of a New Boson at a Mass of 125 GeV with the CMS Experiment at the LHC. *Physics Letters B*, 716:30–61, Sep 2012.

15 J. H. Christenson, J. W. Cronin, V. L. Fitch, and R. Turlay. Evidence for the 2π decay of the k_2^0 meson. *Physical Review Letters*, 13:138–140, Jul 1964.

16 CDF Collaboration. Search for charged Higgs bosons from top quark decays in $p\bar{p}$ collisions at $\sqrt{s} = 1.96$ TeV. *Physical Review Letters*, 96:042003, Feb 2006.

17 CMS Collaboration. Integrated luminocity of CERN. https://twiki.cern.ch/twiki/bin/view/CMSPublic/LumiPublicResults. Accessed 19 June 2020.

18 CMS Collaboration. *CMS TriDAS project: Technical Design Report, Volume 1: The Trigger Systems*. Number CERN-LHCC-2000-038 in Technical Design Report CMS. Dec 2000.

19 CMS Collaboration. The CMS experiment at the CERN LHC. *Journal of Instrumentation*, 3(08):S08004–S08004, Aug 2008.

20 CMS Collaboration. Performance of CMS muon reconstruction in pp collision events at $\sqrt{s} = 7$ TeV. *Journal of Instrumentation*, 7(10):P10002–P10002, Oct 2012.

21 CMS Collaboration. CMS L1 Calorimeter Trigger performance in 2016 data. (CMS-DP-2016-044), Jul 2016.

22 CMS Collaboration. Reconstruction and identification of tau lepton decays to hadrons and tau neutrino at CMS. *Journal of Instrumentation*, 11(01):P01019–P01019, Jan 2016.

23 CMS Collaboration. The CMS trigger system. *Journal of Instrumentation*, 12(01):P01020–P01020, Jan 2017.

24 CMS Collaboration. Particle-flow reconstruction and global event description with the CMS detector. *Journal of Instrumentation*, 12(CMS-PRF-14-001. CMS-PRF-14-001-004. 10):P10003. 82 p, Jun 2017.

25 CMS Collaboration. An embedding technique to determine genuine $\tau\tau$ backgrounds from CMS data. Technical Report CMS-PAS-TAU-18-001, CERN, Geneva, Nov 2018.

26 CMS Collaboration. Performance of missing transverse momentum in pp collisions at sqrt(s)=13 TeV using the CMS detector. (CMS-PAS-JME-17-001), Jul 2018.

27 LHC Higgs cross section Working Group Collaboration. Handbook of LHC Higgs cross sections: 4. Deciphering the nature of the Higgs sector. *arXiv.org*, arXiv:1610.07922, Oct 2016.

28 A. Djouadi. The anatomy of electro-weak symmetry breaking. ii: The Higgs bosons in the Minimal Supersymmetric Model. *Physics Reports*, Mar 2005.

29 F. Englert and R. Brout. Broken symmetry and the mass of gauge vector mesons. *Physical Review Letters*, 13:321–323, Aug 1964.

30 L. D. Faddeev and V. N. Popov. Feynman Diagrams for the Yang-Mills Field. *Physics Letters B*, 25:29–30, Jul 1967.

31 P. Fayet and J. Iliopoulos. Spontaneously Broken Supergauge Symmetries and Goldstone Spinors. *Physics Letters B*, 51:461–464, Sep 1974.

32 Y. Fukuda, T. Hayakawa, E. Ichihara, K. Inoue, K. Ishihara, H. Ishino, Y. Itow, T. Kajita, J. Kameda, S. Kasuga, K. Kobayashi, Y. Kobayashi, Y. Koshio, M. Miura, M. Nakahata, S. Nakayama, A. Okada, K. Okumura, N. Sakurai, and A. Suzuki. Evidence for oscillation of atmospheric neutrinos. *Physical Review Letters*, 81, Aug 1998.

33 J. F. Gunion and H. E. Haber. CP-conserving two-Higgs-doublet model: The approach to the decoupling limit. *Physical Review D*, 67:075019, Apr 2003.

34 G. S. Guralnik, C. R. Hagen, and T. W. B. Kibble. Global conservation laws and massless particles. *Physical Review Letters*, 13:585–587, Nov 1964.

35 R. Harlander, M. Krämer, and M. Schumacher. Bottom-quark associated Higgs-boson production: reconciling the four- and five-flavour scheme approach. arXiv:1112.3478, Dec 2011.

36 P. W. Higgs. Broken symmetries and the masses of gauge bosons. *Physical Review Letters*, 13:508–509, Oct 1964.

37 S. Laurila. *Search for Charged Higgs Bosons Decaying to a Tau Lepton and a Neutrino with the CMS Experiment*. PhD thesis, U. Helsinki (main), Oct 2019.

38 T. D. Lee. A theory of spontaneous t violation. *Physical Review D*, 8:1226–1239, Aug 1973.

39 S. P. Martin. A supersymmetry primer (published in Perspectives on supersymmetry, edited by G. L. Kane). arXiv:hep-ph/09709356, Sep 1997.

40 MissMJ. Standard model of elementary particles. https://en.wikipedia.org/wiki/Standard_Model#/media/File:Standard_Model_of_Elementary_Particles.svg. Accessed 10 April 2020.

41 E. Mobs. The CERN accelerator complex - 2019. Complexe des accélérateurs du CERN - 2019. https://cds.cern.ch/record/2684277, Jul 2019. Accessed 19 June 2020.

42 L. Nanni. Fermi theory of beta decay: A first attempt at electroweak unification. *Advanced Studies in Theoretical Physics*, 13:281, Jul 2019. Original paper in Italian, 1933.

43 I. Neutelings. CMS coordinate system. https://wiki.physik.uzh.ch/cms/latex:example_spherical_coordinates, licenced under CC BY-SA 4.0. Accessed 19 June 2020.

44 T. Sakuma and T. McCauley. Detector and event visualization with SketchUp at the CMS experiment. https://cds.cern.ch/record/1626816. Accessed 19 June 2020.

45 U. Sarkar. *Particle and astroparticle physics, 1st edition.* CRC Press, 2009.

46 A. M. Sirunyan, A. Tumasyan, W. Adam, F. Ambrogi, E. Asilar, T. Bergauer, J. Brandstetter, M. Dragicevic, J. Erö, et al. Search for charged Higgs bosons in the H$\pm \rightarrow \tau \pm \nu$ decay channel in proton-proton collisions at $\sqrt{s} = 13$ TeV. *Journal of High Energy Physics*, 2019(7), Jul 2019.

47 S. Summers and A. Rose. Kalman filter track reconstruction on FPGAs for acceleration of the High Level Trigger of the CMS experiment at the HL-LHC. *EPJ Web of Conferences*, 214:01003, 01 2019.

48 G. 't Hooft. Renormalization of massless Yang-Mills fields. *Nuclear Physics B33: 173-99(1971)*, (1), Jan 1971.

49 A. Tapper and D. Acosta. CMS Technical Design Report for the Level-1 Trigger Upgrade. Technical Report CERN-LHCC-2013-011. CMS-TDR-12, Jun 2013.

50 X. Tata and H. Baer. Weak scale supersymmetry. *Cambridge, UK: Cambridge University Press, 2012*, Mar 2012.

51 H. Waltari. *Higgs bosons as probes of nonminimal supersymmetric models.* PhD thesis, University of Helsinki, Finland, May 2017.

52 J. Wittmann, B. Arnold, H. Bergauer, M. Jeitler, T. Matsushita, D. Rabady, B. Rahbaran, and C.-E. Wulz. The upgrade of the CMS global trigger. *Journal of Instrumentation*, 11(02):C02029–C02029, Feb 2016.